Probing star formation and ISM properties using galaxy disk inclination. I. Evolution in disk opacity since z ~ 0.7

Leslie, S. K.; Sargent, M. T.; Schinnerer, E.; Groves, B.; van der Wel, Arjen; Zamorani, G.; Fudamoto, Y.; Lang, P.; Smolčić, Vernesa

Permanent link / Trajna poveznica: https://urn.nsk.hr/urn:nbn:hr:217:656958

Download date / Datum preuzimanja: **2024-04-26**

Repository / Repozitorij:

Repository of the Faculty of Science - University of Zagreb

Astronomy & Astrophysics

Probing star formation and ISM properties using galaxy disk inclination

I. Evolution in disk opacity since $z \sim 0.7$

S. K. Leslie[1,⋆], M. T. Sargent[2], E. Schinnerer[1], B. Groves[3], A. van der Wel[1], G. Zamorani[4], Y. Fudamoto[5], P. Lang[1], and V. Smolčić[6]

[1] Max-Planck-Institut für Astronomie, Königstuhl 17, 69117 Heidelberg, Germany
e-mail: `leslie@mpia.de`
[2] Astronomy Centre, Department of Physics and Astronomy, University of Sussex, Brighton BN1 9QH, UK
[3] Research School of Astronomy and Astrophysics, Australian National University, Canberra ACT 2611, Australia
[4] INAF-Osservatorio Astronomico di Bologna, via Gobetti 93/3, 40129 Bologna, Italy
[5] Observatoire de Genève, 51 Ch. des Maillettes, 1290 Versoix, Switzerland
[6] Faculty of Science University of Zagreb, Bijenička c. 32, 10002 Zagreb, Croatia

ABSTRACT

Disk galaxies at intermediate redshift ($z \sim 0.7$) have been found in previous work to display more optically thick behaviour than their local counterparts in the rest-frame B-band surface brightness, suggesting an evolution in dust properties over the past ~6 Gyr. We compare the measured luminosities of face-on and edge-on star-forming galaxies at different wavelengths (Ultraviolet (UV), mid-infrared (MIR), far-infrared (FIR), and radio) for two well-matched samples of disk-dominated galaxies: a local Sloan Digital Sky Survey (SDSS)-selected sample at $z \sim 0.07$ and a sample of disks at $z \sim 0.7$ drawn from Cosmic Evolution Survey (COSMOS). We have derived correction factors to account for the inclination dependence of the parameters used for sample selection. We find that typical galaxies are transparent at MIR wavelengths at both redshifts, and that the FIR and radio emission is also transparent as expected. However, reduced sensitivity at these wavelengths limits our analysis; we cannot rule out opacity in the FIR or radio. Ultra-violet attenuation has increased between $z \sim 0$ and $z \sim 0.7$, with the $z \sim 0.7$ sample being a factor of ~3.4 more attenuated. The larger UV attenuation at $z \sim 0.7$ can be explained by more clumpy dust around nascent star-forming regions. There is good agreement between the fitted evolution of the normalisation of the SFR_{UV} versus $1 - \cos(i)$ trend (interpreted as the clumpiness fraction) and the molecular gas fraction/dust fraction evolution of galaxies found out to $z < 1$.

Key words. galaxies: evolution – opacity – galaxies: ISM – galaxies: star formation

1. Introduction

Dust grains in the interstellar medium (ISM) absorb and scatter light emitted by stars and re-emit radiation in the infrared (IR). Dust often has a large impact on star formation rate (SFR) measurements; for example, global galaxy ultraviolet (UV) fluxes usually suffer from 0 to 3 magnitudes of extinction (Buat & Xu 1996). For global galaxy measurements, the term attenuation is used as it refers to the integrated property of an extended distribution, rather than extinction along a line of sight. Dust attenuation depends on the amount and distribution of dust in a galaxy.

Galaxy opacity comes mainly from the presence of dust and is therefore highly dependent on the amount of dust, the dust geometry with respect to the stars, the wavelength of light under consideration, and the optical properties of the dust grains. Dust exists in spiral galaxies and its distribution can be studied through dust emission in the infrared. Dust has been found out to radial distances 1–2 times the optical radius R_{25} of local galaxies (Smith et al. 2016; Hunt et al. 2015; De Geyter et al. 2014; Ciesla

et al. 2012). Although it also exists on the outskirts of galaxies, the dust distribution has been found to have a lower scale height than the stars (Xilouris et al. 1999).

Most current models of galaxy dust distributions include at least two dust components: a distribution of diffuse dust and a distribution of optically thick dust clouds at the site of young star-forming regions (Draine & Li 2007; Galliano et al. 2011; Jones et al. 2013). The diffuse dust is heated by a combination of young and old stars and plays a major role in the total output of dust emission (Ciesla et al. 2014; Bendo et al. 2012, 2010; Boquien et al. 2011; Popescu et al. 2011; Draine & Li 2007; Mathis 1990). Observations have indicated that the face-on opacity of the diffuse dust decreases with radius (e.g. Boissier et al. 2004, 2007; Popescu et al. 2005; Holwerda et al. 2005; Pérez-González et al. 2006; Muñoz-Mateos et al. 2009). The diffuse component dominates the dust emission at longer wavelengths ($\lambda > 160 \, \mu\text{m}$; Dale et al. 2007; Draine et al. 2007; De Vis et al. 2017). The second important component comes from dust in the birth clouds of massive stars (Charlot & Fall 2000; da Cunha et al. 2008). Dust in birth clouds will experience the strong UV radiation from the young stars, with a radiation field 10–100 times more intense than that experienced by the

---

diffuse component (Popescu et al. 2011). Dust emission from these clouds is restricted to the star-forming regions, however it dominates at intermediate wavelengths ($\sim$20–60 μm) (Popescu & Tuffs 2008; Popescu et al. 2011).

In the local Universe, disk galaxies vary from optically thin to thick depending on wavelength and location in the disk (Huizinga & van Albada 1992; Peletier & Willner 1992; Giovanelli et al. 1994, 1995; Jones et al. 1996; Moriondo et al. 1998; González et al. 1998). For example, using the background light technique, studies have found that spiral arms are opaque, but the opacity of the interarm-region decreases with galactic radius (González et al. 1998; White et al. 2000; Keel & White 2001).

A common method to probe the dust opacity, originally proposed by Holmberg (1958, 1975), is to study the inclination dependence of starlight (e.g. Disney et al. 1989; Valentijn 1990; Jones et al. 1996; Tully et al. 1998; Maller et al. 2009; Masters et al. 2010). A disk inclined to our line of sight has higher column density and therefore stellar radiation has to pass through more dust before reaching us, meaning more light is scattered or absorbed. Theoretically, for a completely opaque disk, the surface brightness will not change as a function of inclination angle, but for a transparent disk, the surface brightness will increase as the galaxy becomes edge-on. Luminosity trends give complementary information: for an opaque disk, the luminosity will dim with inclination, whereas for a transparent disk the luminosity should be independent of inclination. This method requires a statistical sample of galaxies. Recently this method has been used by Chevallard et al. (2013) and Devour & Bell (2016) on galaxies in the Sloan Digital Sky Survey (at $z < 0.12$) to measure the difference between edge-on and face-on attenuation in the optical SDSS ugriz passbands as a function of parameters drawn from longer-wavelength surveys that are independent of dust attenuation. Devour & Bell (2016) found that the strength of the relative attenuation varies strongly with both specific SFR and galaxy luminosity (or stellar mass), peaking at $M_* \approx 3 \times 10^{10} M_\odot$. Our work aims to extend these studies by quantifying the inclination–attenuation relationship for wavelengths commonly used to measure SFR: UV, mid-IR (MIR), far-IR (FIR) and radio.

Although studied well locally, the opacity of galaxies as a function of redshift has not been investigated at multiple wavelengths. The Cosmic Evolution Survey (COSMOS) covers an area large enough to obtain a significant number of disk galaxies detected at multiple wavelengths. Taking advantage of the high-resolution *Hubble* Space Telescope (HST) imaging of the COSMOS field, Sargent et al. (2010) were able to study the surface brightness–inclination relation of a morphologically well-defined sample of disk-galaxies at $z \sim 0.7$. A direct comparison of COSMOS spiral galaxies with artificially redshifted local galaxies revealed that the COSMOS galaxies at $0.6 < z < 0.8$ are on average more opaque than local galaxies, having an almost flat rest-frame *B* band surface brightness–inclination relation. Sargent et al. (2010) suggested that this constant relation could be due to the presence of more attenuating material, or a different spatial distribution of dust at $z \sim 0.7$.

In this paper, we extend the analysis of Sargent et al. (2010) to measure the inclination dependence of UV, MIR, FIR, and radio luminosity for a sample of galaxies at $0.6 < z < 0.8$ drawn from the COSMOS survey. We compare these results to what is found using a local sample, matched in galaxy stellar mass and size, drawn from the Sloan Digital Sky Survey (SDSS).

In Sect. 2 we describe the multi-wavelength data sets used and our approach to select a sample of star-forming disk galaxies.

In Sect. 2.3 we derive and apply corrections to measurements of stellar mass, *g*-band half-light radius, and Sérsic index in order to obtain measurements unbiased by dust-related inclination effects. In Sect. 2.4 we show the properties of our sample. We use the inclination-SFR relations to compare the opacity of galaxies in Sect. 3. In Sect. 3.3 we fit our UV results with models of attenuation from Tuffs et al. (2004). In Sect. 3.4 we show that the UV opacity depends on stellar mass surface density. In Sect. 4 we discuss what trends are expected in terms of dust evolution and galaxy opacity at intermediate redshift. Our conclusions are presented in Sect. 5. We find that galaxies show more overall UV attenuation at $z \sim 0.7$, possibly due to a larger fraction of dust that surrounds nascent star-forming regions.

Throughout this work, we use Kroupa (2001) IMF and assume a flat lambda CDM cosmology with (H_0, $\Omega_{\rm M}$, Ω_Λ) = (70 km s^{-1} Mpc^{-1}, 0.3, 0.7).

2. Data and sample selection

To study the inclination dependence of attenuation, we must rely on samples of galaxies that differ only in their viewing angle (Devour & Bell 2016). To achieve a sample of such galaxies both locally and at intermediate redshift ($z \sim 0.7$), we select galaxies from the SDSS and COSMOS survey regions of the sky, respectively.

High-resolution imaging is required to accurately fit a model galaxy brightness profile. Following Sargent et al. (2010), we choose to compare a sample at $z \sim 0.7$ with a local sample ($z \sim 0$), because the central wavelength of the SDSS *g* band matches the rest-frame wavelengths of objects observed in the F814W filter at redshift $z \sim 0.7$ (Kampczyk et al. 2007).

At both $z \sim 0$ and $z \sim 0.7$ we selected star-forming galaxies with stellar masses $\log(M_*/M_\odot) > 10.2$, *g*-band half-light radii $r_{1/2} > 5$ kpc, and Sérsic index $n < 1.2$. These cuts were made to minimise selection biases whilst maintaining a reasonable number of galaxies in our $z \sim 0.7$ sample and will be discussed in more detail in the following sub-sections.

2.1. COSMOS 0.6 < z < 0.8 disks

The $z \sim 0.7$ COSMOS sample was selected in a similar manner to Sargent et al. (2010), drawn from the complete sample of galaxies with $I \leq 22.5$ mag listed in the Zurich Structure and Morphology Catalog (ZSMC; available on IRSA[1]).

We have matched the ZSMC with the COSMOS2015 photometric catalogue of Laigle et al. (2016). The COSMOS2015 catalogue is a near-infrared selected catalogue that uses a combined z^{++}YJHK$_{\rm s}$ detection image. The catalogue covers a square of 2 deg^2 and uses images from UltraVISTA-DR2, Subaru/Hyper-Suprime-Cam, *Spitzer*, *Herschel*-PACS and *Herschel*-SPIRE, respectively. Galactic extinction has been computed at the position of each object using the Schlegel et al. (1998) values and the Galactic extinction curve (Bolzonella et al. 2000; Allen 1976).

We use photometric redshifts ($z_{\rm phot}$) and stellar masses in the COSMOS2015 catalogue[2]. Photometric redshifts were calculated using LePhare (Arnouts et al. 2002; Ilbert et al. 2006) following the method of Ilbert et al. (2013). Fluxes from 30 bands extracted from a 3$''$ aperture using SExtractor were used to

calculate the redshift probability distribution. The dispersion of the photometric redshifts for star-forming galaxies with $i_{AB} < 23$ is $\sigma_{\Delta z/(1+z)} < 0.01$.

We limit our sample to $0.6 \leq z_{phot} \leq 0.8$. At a redshift of ~ 0.7 the observed I-band roughly corresponds to the rest frame g-band and the observed NUV-band roughly corresponds to the $z \sim 0.1$ frame FUV, minimising K-corrections and allowing for easy comparison with local samples.

Stellar masses are derived as described in Ilbert et al. (2015), using a grid of synthetic spectra created using the stellar population synthesis models of Bruzual & Charlot (2003).The 90% stellar mass completeness limit for star-forming galaxies in the redshift of our sample ($0.6 < z < 0.8$) is $10^9 M_\odot$ in the UVISTA Deep field (Laigle et al. 2016). We re-scale the stellar masses from a Chabrier IMF to a Kroupa IMF by dividing by 0.92 (Madau & Dickinson 2014).

X-ray detected sources from XMM-COSMOS (Cappelluti et al. 2007; Hasinger et al. 2007; Brusa et al. 2010) are not included in our analysis because of potential active galactic nuclei (AGN) contamination. We have also checked for MIR-AGN using the Donley et al. (2012) IRAC criteria. Galaxies with associations to multiple radio components at 3 GHz are also excluded because they are radio-AGN (Smolčić et al. 2017a). We select only galaxies classified as star forming in COSMOS2015 which uses the NUV-r/r-J colour–colour selection adapted from the Williams et al. (2009) classification and described in Ilbert et al. (2013).

2.1.1. Morphology information

Morphological measurements were carried out on HST/Advanced Camera for Surveys (ACS) F814W (I-band) images with a resolution of $\sim 0.1''$ (Koekemoer et al. 2007). This corresponds to a physical resolution of ~ 0.67 and 0.75 kpc at redshifts 0.6 and 0.8, respectively. Galaxies are classified as "early type", "late type" or "irregular/peculiar" according to the Zurich Estimator of Structural Types algorithm (ZEST; Scarlata et al. 2007). Late-type galaxies (ZEST Class = 2) are separated into four sub-classes, ranging from bulge-dominated (2.0) to disc-dominated (2.3) systems. For simple comparison with the SDSS galaxies, we select disk galaxies based on Sérsic index $n < 1.2$ (described in Sect. 2.2.1). Increasing the bulge-to-disk ratio at a constant opacity can mimic the effect of increasing the opacity of a pure disk (Tuffs et al. 2004). We have confirmed that our results for the COSMOS sample do not change when selecting pure disks using ZEST Class = 2.3 rather than using Sérsic index.

Galaxies in the ZSMC catalogue have been modelled with single-component Sérsic (1968) profiles using the GIM2D IRAF software package (Simard et al. 2002). In the single-component case, GIM2D seeks the best fitting values for the total flux F_{tot}, the half-light radius $R_{1/2}$, the position angle ϕ, the central position of the galaxy, the residual background level, and the ellipticity $e = 1 - b/a$, where a and b are the semimajor and semiminor axes of the brightness distribution, respectively. See Sargent et al. (2007) for more details on how the surface-brightness fitting was performed. In order not to miss low-surface galaxies, we cut our sample at $r_{1/2} > 4$ kpc (Sargent et al. 2007, see Fig. 12). This is because at a given size a minimum surface brightness is required for a galaxy to meet the $I < 22.5$ criterion of the morphological ZSMC catalogue. Including smaller galaxies biases our sample against low brightness galaxies. Our sample is complete for galaxies with $r_{1/2} > 4$ kpc.

2.1.2. Data used for SFR estimation in the COSMOS field

The multi-wavelength photometry used for measuring SFRs at FUV, MIR, FIR, and radio wavelengths is summarised in Table 1. For the COSMOS data, all fluxes are found in the COSMOS2015 catalogue, except for the radio 3 GHz fluxes which are from Smolčić et al. (2017a).

At $z = 0.7$, the GALEX NUV filter roughly corresponds to the FUV filter at $z = 0.1$. The COSMOS field was observed as part of the Galaxy Evolution Explorer (GALEX) Deep Imaging Survey (DIS) in the Far-UV (~ 1500 Å) and Near-UV (~ 2300 Å).

We also draw 100 μm fluxes from the COSMOS2015 catalogue. These data were taken with Photoconductor Array Camera and Spectrometer (PACS; Poglitsch et al. 2010) on the *Herschel* Space Observatory through the PACS Evolutionary Probe (PEP) guaranteed time program (Lutz et al. 2011). Source extraction was performed by a point spread function (PSF) fitting algorithm using the 24 μm source catalogue to define prior positions.

The VLA-COSMOS 3 GHz Large Project catalogue (Smolčić et al. 2017b) contains 10830 radio sources down to 5 sigma (and imaged at an angular resolution of 0.74''). These sources were matched to COSMOS2015 (as well as other multi-wavelength COSMOS catalogues) by Smolčić et al. (2017a).

2.2. Local $0.04 < z < 0.1$ disks in SDSS

The local sample is drawn from the SDSS Data Release 7 (Abazajian et al. 2009). In particular, we select galaxies with publicly available redshifts, stellar masses, and emission line fluxes from the spectroscopic MPA/JHU catalogue[3] described in Brinchmann et al. (2004). We select galaxies in the redshift range $0.04 < z < 0.1$. The lower redshift limit is to ensure that the SDSS fibre covers at least 30% (median coverage 38%) of the typical galaxy to minimise aperture effects (Kewley et al. 2005). The sample is constrained to $z < 0.1$ to avoid incompleteness and significant evolutionary effects (Kewley et al. 2006) and to ensure that the FUV passband lies above the numerous stellar absorption features that occur below 1250 Å.

Total stellar masses were calculated by the MPA/JHU team from ugriz galaxy photometry using the model grids of Kauffmann et al. (2003) assuming a Kroupa IMF. The stellar masses in the MPA/JHU catalogue have been found to be consistent with other estimates (see Taylor et al. 2011; Chang et al. 2015). In the following analysis, we use the median of the probability distribution to represent each parameter, and the 16th and 84th percentiles to represent the dispersion.

We further limit our sample to galaxies classified as "star-forming" ($\log([OIII]/H\beta) < 0.7 - 1.2(\log([NII]/H\alpha) + 0.4)$) or "starburst" (the galaxy is "starforming" but also has an $H\alpha$ equivalent width >50 Å). In this way, we exclude quiescent galaxies and galaxies whose optical emission is dominated by an AGN. We also exclude any galaxies that are classified as AGN based on their WISE colours following Mateos et al. (2012).

2.2.1. Morphology information

Simard et al. (2011) provide morphological information that is consistent with the data provided by Sargent et al. (2007) used for this paper. Simard et al. (2011) performed two-dimensional (2D) point-spread-function-convolved model fits in the g and r band-passes of galaxies in the SDSS data release 7. The faint

---

[3] http://www.mpa-garching.mpg.de/SDSS/DR7/

Table 1. Data used for SFR estimation.

Wavelength	Instrument	Survey	Ω (deg^2)	3σ (μJy)	N_{gals}	References
COSMOS UV	GALEX (NUV)	DIS	1.7	0.23	296	(1)
COSMOS MIR	*Spitzer*-MIPS (24 μm)	S-COSMOS	1.7	43	373	(2,3)
COSMOS FIR	*Herschel*-PACS (100 μm)	PEP	1.7	5000	87	(4,5)
COSMOS Radio	VLA (*S*-band, 3 GHz)	VLA-COSMOS 3 GHz	1.7	7	58	(6,7)
SDSS UV	GALEX (FUV)	MIS	$\sim$1000	1.8	1003	(8)
SDSS MIR	WISE (W3, 12 μm)	AllWISE	$\sim$8400	340	8333	(9,10)
SDSS FIR	IRAS (60 μm)	FSC	$\sim$8400	1.2×10^5	291	(11)
SDSS Radio	VLA (*L*-band, 1.4 GHz)	FIRST, NVSS	$\sim$8400	450	198	(12,13,14)

Notes. The area Ω quoted is the overlap between the particular wavelength and the SDSS or ACS surveys from which the morphological parameters are drawn. N_{gals} is the number of galaxies in our sample detected at each wavelength with robust mass, inclination, and SFR measurements (signal-to-noise ratio (S/N) >3).
References. (1) Capak et al. (2007); (2) Sanders et al. (2007); (3) Le Floc'h et al. (2009); (4) Poglitsch et al. (2010); (5) Lutz et al. (2011); (6) Smolčić et al. (2017b); (7) Smolčić et al. (2017a); (8) Bianchi et al. (2011); (9) Wright et al. (2010); (10) Chang et al. (2015); (11) Moshir & et al. (1990); (12) Kimball & Ivezić (2014); (13) Becker et al. (1995); (14) Condon et al. (1998).

surface brightness limit of the spectroscopic sample was set to $\mu_{50} = 23.0$ mag arcsec^{-2} for completeness. The SDSS images have a typical seeing of 1.4″ (Simard et al. 2011). This corresponds to a physical resolution of 1.1 kpc and 2.6 kpc at $z = 0.04$ and 0.1, respectively. We use the SDSS g-band GIM2D single Sérsic model fitting results in order to match the rest frame wavelength and model used to derive COSMOS morphological parameters.

To select disk-dominated galaxies, we restrict our sample to galaxies that have a g-band Sérsic index $n < 1.2$. This is motivated by Sargent et al. (2007); in particular, their Fig. 9, which shows that pure disk galaxies (ZEST type 2.3) have in general $n < 1.2$.

2.2.2. Data used for SFR estimation in the SDSS field

The catalogues used for measuring SFRs in our local sample are listed in Table 1 as well as some information regarding the instruments used, the sky coverage, and average noise properties. For all wavelengths, we require a S/N of at least three for the fluxes to be used in our analysis.

We make use of FUV data from the GALEX Medium Imaging Survey (MIS) that has been cross-matched with the SDSS DR7 photometric catalogue by Bianchi et al. (2011). We correct the GALEX photometry for galactic reddening following Salim et al. (2016) who use the extinction coefficients from Peek & Schiminovich (2013) for UV bands:

$$A_{\mathrm{FUV}} = 10.47 E(B-V) + 8.59 E(B-V)^2 - 82.2 E(B-V)^3, \quad (1)$$

where $E(B-V)$ are the galactic colour-excess values.

We use observations taken by the Wide-field Infrared Survey Explorer (WISE; Wright et al. 2010) telescope to probe the MIR emission of our local galaxy sample. Specifically, we rely on the catalogue compiled by Chang et al. (2015) which contains a match of SDSS galaxies (in the New York University Value-Added Galaxy Catalog; Blanton et al. 2005; Adelman-McCarthy 2008; Padmanabhan et al. 2008) with sources in the AllWISE catalogue. Fluxes were measured using the profile-fitting method that assumes the sources are unresolved and has the advantage of minimising source blending. Chang et al. (2015) found that most galaxies are typically smaller than the PSF, but results from their simulation showed that there is a difference between the true flux and the PSF flux which is a function of the effective radius (R_e of

the Sérsic profile) and this difference is independent of the input flux, axis ratio, or n. Therefore, we use their flux values that have been corrected based on R_e.

Long wavelength infrared data were obtained from the Infrared Astronomical Satellite (IRAS) Faint Source Catalog (FSC) v2.0. (Moshir & et al. 1990). We match the FSC to our parent SDSS sample using the `Sky Ellipses` algorithm in `Topcat` because the IRAS source position uncertainties are significantly elliptical. We match using the 2σ positional uncertainty ellipse of the IRAS sources and assume a circular positional uncertainty on each SDSS source of 1″.

We make use of the radio continuum flux densities compiled in the Unified Radio Catalogue v2 (Kimball & Ivezić 2008, 2014). The catalogue was constructed by matching two 20 cm (1.4 GHz) surveys conducted with the Very Large Array (VLA): FIRST (Faint Images of the Radio Sky at Twenty Centimeters; Becker et al. 1995) and NVSS (NRAO-VLA Sky Survey; Condon et al. 1998). The FIRST survey has an angular resolution of ∼5″ and a typical rms of 0.15 mJy/beam. The NVSS survey, on the other hand, has an angular resolution of ∼45″ and a typical rms of 0.45 mJy/beam. We use sources with a ≤2″ separation between the FIRST and SDSS positions as recommended by Ivezić et al. (2002) and Kimball & Ivezić (2014). For our analysis, we use the 1.4 GHz fluxes from the NVSS catalogue because it is better suited for measuring the global flux from a galaxy than the FIRST survey due to the more compact observing configuration.

2.3. Inclination-independent sample selection

Devour & Bell (2016) describe some of the many potential selection effects which could affect the results of an inclination-dependent study such as ours. If any of the parameters used in our selection, such as stellar mass or radius, is dependent on inclination, then we might get a false signal. We show the relationship between the parameters used for our sample selection and galaxy inclination in Fig. 1.

The inclination is calculated from axis ratios measured from the rest-frame g-band image using the Hubble (1926) formula

$$\cos^2(i) = \frac{(b/a)^2 - (b/a)^2_{\mathrm{min}}}{1 - (b/a)^2_{\mathrm{min}}}, \quad (2)$$
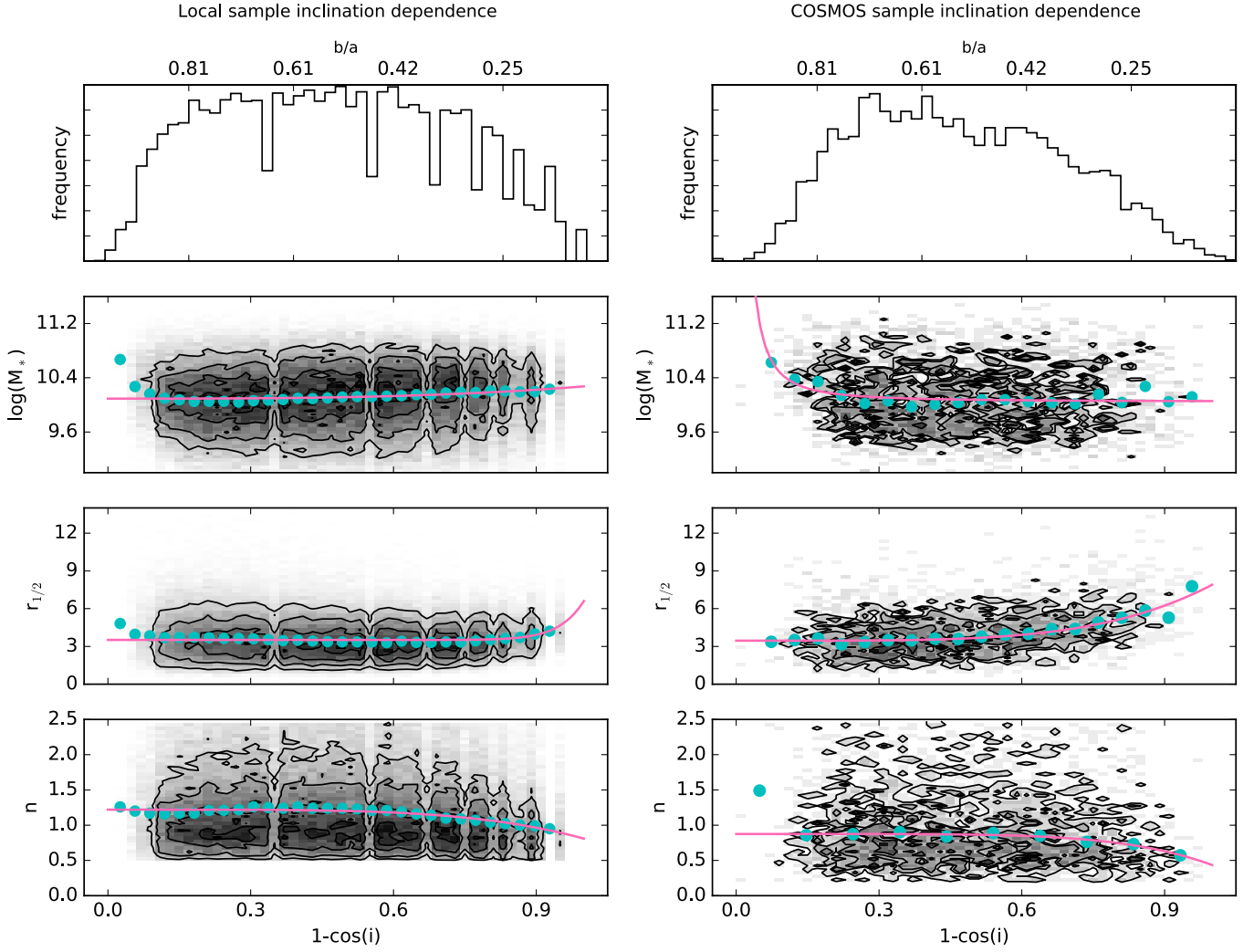
Fig. 1. Relationship between parameters used for sample selection (stellar mass $M_*[M_\odot]$, half-light radius in rest-frame g-band $r_{1/2}$ [kpc], and Sérsic index n) with inclination (in the form of $1 - \cos(i)$). The distributions are shown for galaxies in our parent samples (see Sects. 2.1., 2.2., and 2.3). A histogram of the inclination distribution (or equivalently axis ratio distribution) is shown in the *top panels*. Galaxies randomly oriented would produce a flat distribution. Dips in the local b/a distribution are caused by numerical issues in the Simard et al. (2011) fitting. Teal dots trace the median values in bins of inclination and the pink curves show the resulting power-law fit (Eq. (3)) to the medians. We subtract the inclination dependent term from our parameters before performing our final sample selection to avoid artificially introducing inclination trends in our results.

with $(b/a)_{min} = 0.15$ (following Sargent et al. 2010 and based on Guthrie 1992 and Yuan & Zhu 2004). If galaxies were randomly oriented disks, we would expect to see a flat distribution of $1 - \cos(i)$. This is roughly the case for our local parent sample; however, our COSMOS $z \sim 0.7$ parent sample has a distribution of $1 - \cos(i)$, slightly skewed towards face-on galaxies. Instances of $b/a \sim 1$ and 0 (and hence $1 - \cos(i) = 0$ and 1) are rare due to intrinsic disk ellipticity and the finite thickness of edge-on systems, respectively. The apparent thickness might vary with the apparent size ($R_{1/2}$), with smaller images appearing rounder, even if images are deconvolved with the PSF (Shao et al. 2007). We do not account for this, but it might contribute to the trend we see between inclination and half-light radius in our samples in Fig. 1.

Driver et al. (2007) performed an empirical correction to remove inclination-dependent attenuation effects on the turn-over magnitude in B-band luminosity function. Inspired by this, we fit a power-law,

$$y = k_1[1 - \cos(i)]^{k_2} + y_c, \qquad (3)$$

to our selection parameters, where y is the stellar mass, half-light radius, or Sérsic index. We first calculate the median "y" in bins of $1 - \cos(i)$ (50 bins for the local sample and 20 bins for the COSMOS $z \sim 0.7$ sample) and then find the best fitting parameters k_1, k_2, and y_c using the Python task scipy.optimize.curve_fit (χ^2 minimisation). For this analysis, we include only galaxies that satisfy our constraints on redshift and star-formation activity (see Sects. 2.1 and 2.2), and $n < 4$ (selecting late-type galaxies), which will be referred to as our "parent samples". The fitted parameters are given in Table 2.

In our SDSS sample, there is a trend that more inclined galaxies (those with a low axis ratio) are more likely to have a higher measured stellar mass. On the other hand, in the COSMOS sample, there is no significant ($k_1 = 0$ within the errors) relation between stellar mass and inclination. The stellar masses for our local sample were derived using optical photometry (and spectroscopic redshifts) only, whereas the stellar mass of COSMOS galaxies is derived using 16 photometric bands, including IRAC near-IR data. This might suggest that the mass of the inclined SDSS galaxies is overestimated due to redder optical colours.

Table 2. Fitted parameters that describe the inclination dependence of galaxy properties that we use for sample selection.

y	k_1	k_2	y_c
SDSS $\log(M_*/M_\odot)$	0.18 ± 0.04	3.0 ± 1.4	10.09 ± 0.02
COSMOS $\log(M_*/M_\odot)$	0.01 ± 0.01	-1.6 ± 0.5	10.05 ± 0.04
SDSS $r_{1/2}$ (kpc)	3.1 ± 2.5	19 ± 9	3.52 ± 0.04
COSMOS $r_{1/2}$ (kpc)	4.4 ± 0.4	4.4 ± 0.7	3.5 ± 0.1
SDSS n	-0.41 ± 0.05	4.5 ± 0.7	1.22 ± 0.01
COSMOS n	-0.44 ± 0.05	5.6 ± 1.2	0.87 ± 0.01

Notes. We fit the relation $y = k_1[1 - \cos(i)]^{k_2} + y_c$ to our parent samples of star-forming galaxies based on the SDSS and COSMOS surveys.

We find that the most important inclination effect is that on galaxy size, $r_{1/2}$. Authors such as Yip et al. (2010); Huizinga & van Albada (1992); Möllenhoff et al. (2006); Masters et al. (2010) and Conroy et al. (2010) have all previously reported that galaxy size measurements (such as half-light or effective radius) are dependent on galaxy axis ratio b/a, with edge-on galaxies appearing larger at a fixed magnitude. Our local results are consistent with results from Möllenhoff et al. (2006) who show that the B-band sizes increase by 10–40% from face-on to edge-on due to a reduction of the light concentration by centrally concentrated dust in local galaxies. Our fit for the dependence of radius on inclination for the COSMOS sample results in a size increase of 110% when i is increased from 0 to 88 degrees. However, the large correction only applies at high inclination ($b/a < 0.3$, $i > 75$ deg).

Maller et al. (2009) and Patel et al. (2012) found that inclination corrections have a strong dependence on Sérsic index (in the u band and UVJ bands, respectively). Having even a small bulge will reduce the ellipticity of the isophotes of a galaxy, resulting in a deficiency of galaxies with $b/a \sim 0$. We can see this trend in the spread of inclination values at a given n in Fig. 2. The distribution of n has a large tail of high n-values which cause even our fit to the median n values to pass above the mode of the distribution.

During our sample selection we account for the inclination dependence using our determined fit values (Table 1) and Eq. (3). We subtract the inclination-dependent term to correct parameters to their face-on equivalent. To summarise we select galaxies with

- $n_{corr} < 1.2$

- $r_{1/2,corr} > 4$ kpc

- $\log\left(\frac{M_*}{M_\odot}\right)_{corr} > 10.2$.

2.4. Sample properties

Figure 2 shows the distribution of relevant properties for galaxies in the local sample (left) and the COSMOS $z \sim 0.7$ sample (right) after the selection cuts detailed in the previous section were applied. Each histogram shows the distribution of galaxies detected at a particular wavelength. The total number of galaxies in each subsample is indicated in Table 1.

The distribution of $\cos(i)$, where i is the inclination, is shown in the top panels of Fig. 2. As mentioned above, a sample of randomly oriented thin disks should produce a constant ($1 - \cos(i)$) distribution. In the local sample, galaxies detected in FIR, MIR, and UV catalogues have very similar (flat) distributions of galaxy inclination ($1 - \cos(i)$). In both the local and COSMOS sample, the inclination distribution of radio-detected galaxies is

skewed towards more inclined galaxies. In the COSMOS sample, the FIR-detected subsample is also skewed towards more inclined galaxies. It is possible that this skewness is caused by a surface-brightness effect – for a fixed global flux limit, an edge-on galaxy will have a higher surface brightness than a face-on galaxy because the area on the sky is smaller ($\propto \sin(i)$). This effect is true especially in the radio, which is unobscured by dust[4].

The distributions of redshifts in the COSMOS field are similar for the different wavelengths. Locally, the FIR sample peaks at lower redshifts because of the limited sensitivity of the IRAS catalogue. The number of galaxies of the UV and MIR subsamples increases with redshift in our local sample as an increasing volume of space is sampled.

The third panels show the half-light radius distributions of the sample after inclination correction. The local galaxy sample has a median $r_{1/2,corr} = 5.04$ kpc, whereas the COSMOS sample has a median of $r_{1/2,corr} = 5.25$ kpc. The size distributions of the different subsamples are consistent.

The distribution of Sérsic index, n, is shown in the fourth row of Fig. 2. For our sample, we selected galaxies with $n < 1.2$. The distribution of n for local galaxies does not go below 0.5 because this was the lowest n value allowed by Simard et al. (2011) in their pure Sérsic profile model fits. The distribution of n for local galaxies peaks at higher values than the distribution at $z \sim 0.7$. This could be due to star-forming galaxies becoming more mature over time (Scoville et al. 2013).

The stellar mass distributions (Fig. 2, bottom row) show some important biases between the subsamples. For the COSMOS sample, the radio and FIR subsamples are peaked at larger stellar masses than the UV and MIR subsamples. In the local sample the FIR $\log(M_*)$ distribution starts to fall off at lower stellar masses due to the shallow detection limit of IRAS survey and the correlation between stellar mass and galaxy luminosity. Adopting the relationship between SFR and stellar mass (Eq. (4)), the local FIR observations can only detect a main sequence galaxy with $\log(M_*/M_\odot) > 10.2$ at $z \sim 0.04$. For this calculation, a galaxy with SFR 0.3 dex (1σ) below the MS given in Sect. 3 was considered. Similarly, the COSMOS FIR observations are complete down to $\log(M_*/M_\odot) > 10.4$ at $z \sim 0.6$.

2.5. SFR estimates

To calculate SFR, we use the UV and TIR calibrations compiled in Kennicutt & Evans (2012). These calibrations assume

---

[4] We found more galaxies with larger b/a when considering NVSS detected sources compared to FIRST detected sources, but this difference was not statistically significant.
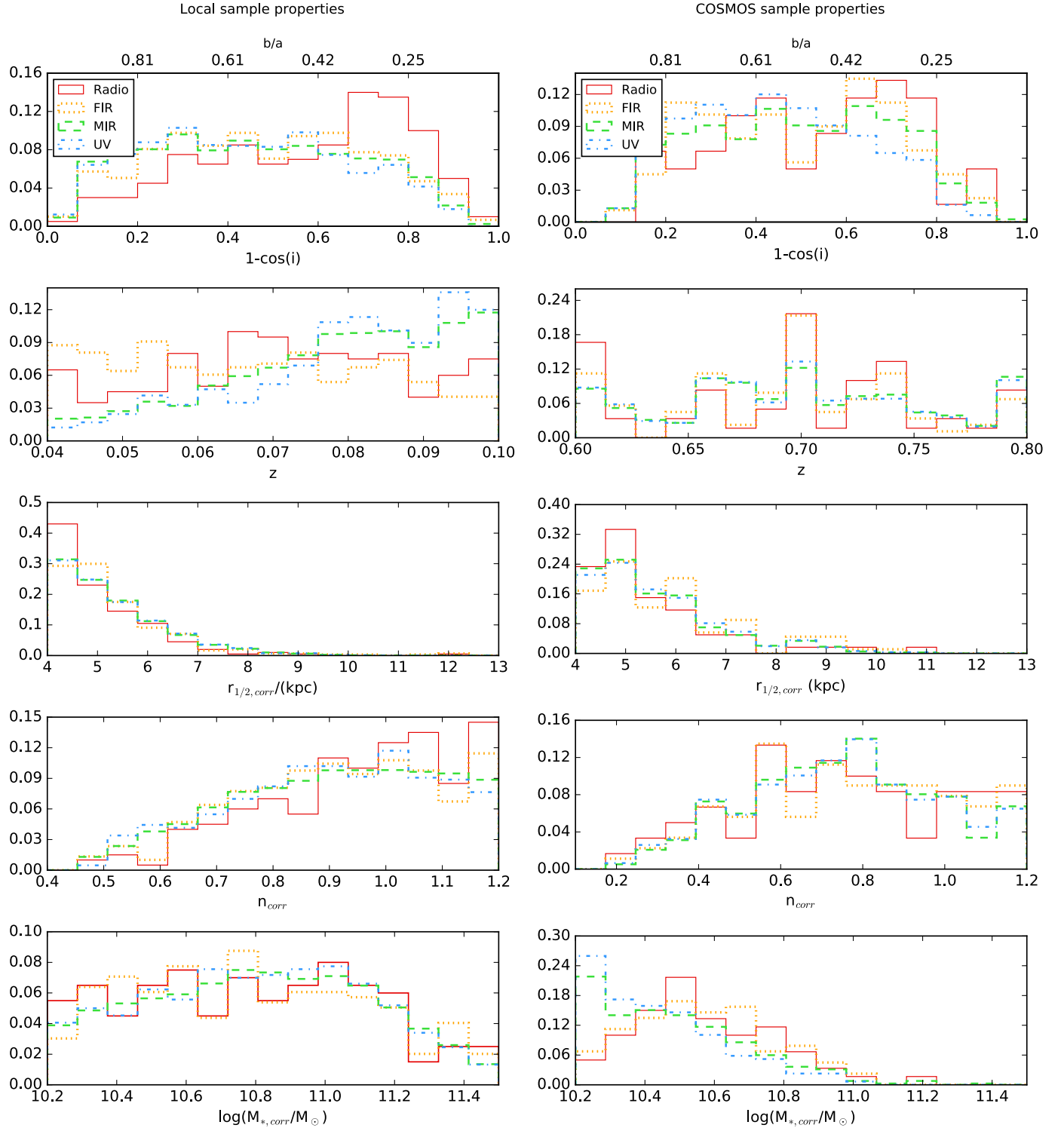
Fig. 2. Normalised histograms of the galaxy properties of our multi-wavelength sub-samples after selection cuts. Histograms show the inclination-corrected values for $r_{1/2}$, n (derived from single Sérsic profile fits to rest-frame g-band light profiles), and $\log(M_*)$. The y-axis shows the fraction of galaxies (in that subsample) in each bin. Radio-detected galaxies have a distribution of optical axis-ratios skewed towards edge-on galaxies.

a Kroupa IMF and a constant star formation rate. Star formation rates are given in units of $M_\odot$ yr^{-1}.

Young stars emit the bulk of their energy in the rest-frame UV. The FUV emission from star-forming galaxies is dominated by radiation from massive O and B stars. We use the SFR calibration derived for the GALEX FUV bandpass to calculate SFR$_{\rm UV}$ for our local sample (see Table 1 of Kennicutt & Evans

2012). At $z = 0.7$ the GALEX NUV filter samples approximately the same rest-frame wavelength as the GALEX FUV filter at $z = 0.1$ (Zamojski et al. 2007). The GALEX NUV flux is used with the local FUV calibration. No correction for dust attenuation is applied. FUV attenuation corrections and their inclination dependence will be discussed in Paper II of this series.

For both the MIR and FIR monochromatic tracers, we convert the monochromatic flux density to the total infrared luminosity (8–1000 μm) using the Wuyts et al. (2008) spectral energy distribution (SED) template and then calculate the SFR using the L_{IR} calibration of Murphy et al. (2011). The Wuyts et al. (2008) template was constructed by averaging the logarithm of the Dale & Helou (2002) templates resulting in a SED shape reminiscent of M82 (Wuyts et al. 2011a). Wuyts et al. (2008 and 2011b) use their template to derive L_{IR} from monochromatic IR bands and show that the 24 μm-derived SFR is consistent with a multiband FIR SFR over $0 < z < 3$. The SED is valid for MS galaxies; however, the use of a single template for all the galaxies may introduce some scatter in the estimate of the FIR luminosity.[5] We do not use templates that rely on a priori knowledge of the SFR and distance from the MS (such as e.g. Magdis et al. 2012) because the SFRs could be biased due to inclination effects (see e.g. Morselli et al. 2016 on how galaxy inclination impacts the measured scatter of the MS).

We calculate the luminosity density L_ν, in a given filter following da Cunha et al. (2008). For the IRAS and *Spitzer*/IRAC photometric systems, the convention is to use the calibration spectrum $\nu C_\nu = \lambda C_\lambda = $ constant (see Beichman et al. 1988 and the IRAC data Handbook[6]). The *Spitzer*/MIPS system was calibrated using a black body spectrum of temperature 10 000 K, such that $C_\lambda = B_\lambda(10\,000\,\text{K})$ (MIPS Data Handbook[7]). For the WISE system we assume $C = 1$[8]. For each galaxy, we redshift the SED and convolve it with the appropriate filter response to determine the expected measured luminosity. We then scale the SED to match the measured single-band luminosity and integrate the scaled SED between 8 and 1000 μm (rest-frame) to obtain the total infrared luminosity.

Locally we use the corrected WISE 12 μm fluxes from Chang et al. (2015) to calculate SFR$_{MIR}$. At $z = 0.7$, we use MIPS 24 μm fluxes, which correspond to a rest-frame 14 μm flux. We use IRAS 60 μm luminosity to probe SFR$_{FIR}$ of local galaxies, as it probes near the peak of the dust SED. For galaxies in our COSMOS sample, we use the observed 100 μm PACS data, which correspond to rest frame $\sim$60 μm. Filter responses were obtained from the SVO Filter Profile Service[9]. WISE 12 μm luminosities have been observed to correlate well with Hα SFR (Lee et al. 2013; Cluver et al. 2014) above solar metallicity.

To calculate radio-SFRs in our local SDSS sample, we use empirical 1.4 GHz SFR calibration derived recently by Davies et al. (2017) for star-forming galaxies in the Galaxy and Mass Assembly (GAMA; Driver et al. 2011) and FIRST surveys. We use the calibration anchored to the UV+TIR SFR (after converting from a Chabrier to Kroupa IMF by adding 0.025 dex; Zahid et al. 2012). Recently, Molnar et al. (2018) used IR data from *Herschel* and 3 GHz VLA observations for a sample of star-forming galaxies in the COSMOS field to measure the infrared-radio correlation out to $z < 1.5$. Molnar et al. (2018) separated disk-dominated from spheroid-dominated galaxies using the ZEST catalogue. We use their finding that for disk-dominated galaxies, the IR-radio ratio scales as $q_{TIR} \propto (1 + z)^{-0.04\pm0.01}$, and

by relating the radio luminosity to the TIR luminosity, we are able to use the TIR SFR calibration in Kennicutt & Evans (2012).

For a comparison of the SFR tracers used in this work, we refer the reader to Appendix B.

3. Inclination-dependent SFR

In this section, we consider the inclination dependence of galaxy SFRs derived from multiple wavelengths. There are different galaxies included in the different wavelength subsamples. For the local UV sample, this is largely due to the different survey areas. But different emission mechanisms occurring in different galaxies can result in different SED shapes of galaxies, meaning some galaxies are brighter (and detectable) or dimmer (and non-detectable) at particular wavelengths. We have made a size, mass, and Sérsic index cut to select star-forming galaxies to ensure that galaxies do not have drastically different SED shapes for both our local and COSMOS samples. Nonetheless, the different depths of the different observations can bias the subsample towards particular galaxies. For example, the radio and FIR subsamples might select more starburst galaxies with high SFRs due to their shallow depth.

Star-forming galaxies fall on a particular locus in the SFR-stellar mass plane with the logarithmic properties being linearly correlated. We refer to this relation as the star-forming galaxy main sequence (MS; Noeske et al. 2007). The normalisation and (less strongly) slope of the MS have been reported to evolve with redshift, with galaxies at high redshift having higher SFRs at a given mass than local galaxies. The normalisation evolution is thought to reflect the increased amount of cold gas available to galaxies at high redshift (e.g. Tacconi et al. 2013). The average galaxy at a given mass forms more stars at $z \sim 0.7$ than the average galaxy at $z \sim 0$. To place the SFRs of the two samples on a comparable scale, we normalise our multi-wavelength SFRs by the average MS SFR expected for a galaxy with a given stellar mass and redshift. The locus of the MS is known to depend on sample selection (e.g. Karim et al. 2011) and, in particular, on how actively "star forming" the sample under consideration is. We adopt the best-fit MS relation for an updated version (M. Sargent, private communication) of the data compilation presented in Sargent et al. (2014).

$$\log\left(\frac{\text{SFR}_{MS}}{M_\odot \text{yr}^{-1}}\right) = 0.816 \log\left(\frac{M_*}{M_\odot}\right) - 8.248 + 3\log(1 + z). \quad (4)$$

By combining different measurements from the literature that employ different selection criteria, different SF tracers (UV, IR, or radio), and different measurement techniques, Sargent et al. (2014) were able to derive a relation that is representative of the average evolution of the sSFR of main sequence galaxies. The new relation presented in Eq. (4) has been recalculated using recent works such as Chang et al. (2015). However, the IMF (Chabrier 2003) and cosmology (WMAP-7; Larson et al. 2011) assumed by Sargent et al. (2014), differs from ours. To convert the relation from a Chabrier to a Kroupa IMF, we add 0.03 dex to the stellar mass (Madau & Dickinson 2014; Speagle et al. 2014). The different cosmologies will affect the SFR through the square of the luminosity distance for a given redshift. The correction is redshift dependent: for $0.04 < z < 0.1$, we adjust the SFR by -0.004 dex and for $0.6 < z < 0.8$ we adjust the SFR by $+0.006$ dex.

Between $z = 0.07$ and $z = 0.7$ (median redshifts of our two samples) the normalisation changes such that an average $\log(M_*/M_\odot) = 10.5$ main sequence galaxy located exactly at the

---

[5] We have also confirmed that using the MIR SFR calibrations of Battisti et al. (2015) does not qualitatively change our analysis.

[6] http://irsa.ipac.caltech.edu/data/SPITZER/docs/irac/iracinstrumenthandbook/

[7] http://irsa.ipac.caltech.edu/data/SPITZER/docs/mips/mipsinstrumenthandbook/

[8] http://wise2.ipac.caltech.edu/docs/release/allsky/expsup/sec4_4h.html#conv2ab

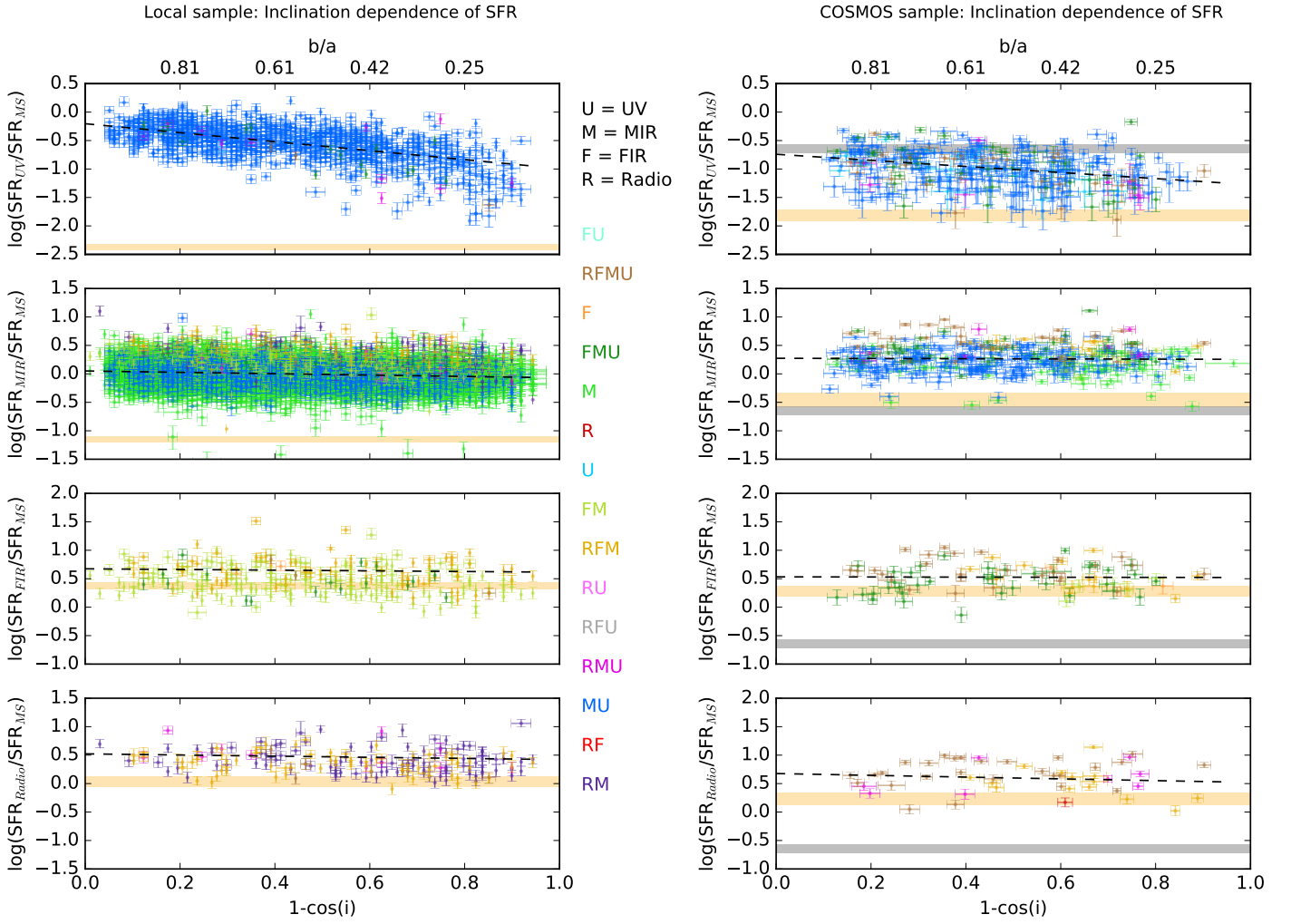[9] http://svo2.cab.inta-csic.es/svo/theory/fps3/index.php?mode=browse

Fig. 3. Inclination dependence of multiwavelength SFRs. y-axis: $\log(\text{SFR}_\lambda) - \log(\text{SFR}_{\text{MS}})$. *Top to bottom*: UV, MIR, FIR, and radio-determined SFR. x-axis: $1 - \cos(i)$, where i is the galaxy inclination. Face-on galaxies are on the left of the plot (at 0) and edge-on galaxies are on the right-hand side (at 1). The *left panels* show SDSS galaxies ($0.04 < z < 0.1$) and the *right panels* show COSMOS galaxies ($0.6 < z < 0.8$). The colour index at the centre indicates which bands were detected; R = radio, F = FIR, M = MIR, and U = UV. The orange shaded region shows the minimum SFR that could be detected across the redshift ranges given the flux limits of the respective surveys. The dashed lines show the median best-fit obtained from 1000 realisations of the data. The grey regions on the *right panels* show where the local ($0.04 < z < 0.1$) main-sequence SFR lies with respect to the main sequence at $z = 0.7$. This shows how the normalisation of the main sequence evolves over our redshift range.

core of the SFR-M_* relation has a SFR of 2.6 $M_\odot$ yr^{-1} at $z = 0.07$ and 11 $M_\odot$ yr^{-1} at $z = 0.7$. We investigate the affects of using different MS relations in Appendix A.

Figure 3 shows the relation $\log(\text{SFR}_\lambda) - \log(\text{SFR}_{\text{MS}})$ with inclination where SFR_{MS} is the main sequence SFR for a galaxy of a given mass. To quantify trends present in Fig. 3, we fit a robust linear model to the data:

$$y = \log(\text{SFR}/\text{SFR}_{\text{MS}}) = \text{slope} \cdot (1 - \cos(i)) + \text{intercept}, \qquad (5)$$

using the statsmodels.api package in Python that calculates an iteratively re-weighted least-squares regression given the robust criterion estimator of Huber (1981).

To estimate the uncertainties in our results, we resampled the data by drawing (with replacement) a new sample of galaxies 1000 times. We then drew the new galaxy inclination and SFR/SFR$_{\text{MS}}$ values from the measurement uncertainty distribution. The COSMOS sample has asymmetric errors in inclination and stellar mass, and the local sample has asymmetric errors inestimate the uncertainties stellar mass. To sample

these asymmetric distributions, we combined two Gaussian distributions with widths given by the upper and lower limits of the error, normalised so that a new sample data-point is equally likely to lie above or below the measurement. Linear regression was performed on each sample drawn, and the best-fitting slopes and intercepts with their uncertainties are shown in Fig. 4.

Projecting the best-fitting parameter pairs in Fig. 4 onto the horizontal and vertical axes, we obtain a distribution of the best fitting slopes and intercepts, respectively. The 50th (median), 5th and 95th percentiles are given in Table 3. The dashed lines in Fig. 3 indicate the median of the fitted parameters.

The flux limits of the surveys correspond to a minimum observable luminosity, and hence SFR, that increases with redshift. We show the SFR that corresponds to this minimum for our redshift ranges coloured in orange in Fig. 3. The limits show that we are limited in our analysis of the FIR and radio-opacity of galaxies both for the local and $z \sim 0.7$ samples, however, they were not taken into account in our fits.

3.1. Slopes: opacity

If disk galaxies are transparent or optically thin then the luminosities and hence SFRs should not depend on inclination angle. In this case, we would see no gradient in Fig. 3. If galaxies are optically thick, or opaque, then the luminosity observed can only originate from the stars at the outer surface visible to our line of sight. The projected area varies with $\cos(i)$ for a circular disk. Therefore, for an opaque galaxy, we expect the measured SFR to decrease with the inclination angle (and $1 - \cos(i)$), producing a negative slope in Fig. 3.

A negative slope is clear in both the local and COSMOS SFR$_{FUV}$ inclination relations. We find that highly inclined galaxies suffer from more FUV attenuation than face-on galaxies, indicating that disk galaxies are optically thick at FUV wavelengths at both redshifts. The fitted values for the slopes are -0.79 ± 0.09 and -0.5 ± 0.2, for the $z \sim 0$ and $z \sim 0.7$ samples.

Davies et al. (1993) explained that when measuring surface-brightness–inclination relations to study disk opacity, a survey limited by surface brightness might not be able to probe a large enough range of surface brightnesses required to detect a slope, even if some opacity is present. Similarly, if the survey is not deep enough to probe a range of luminosities, then we might incorrectly conclude that a lack of slope indicates that the disks are transparent. We find that the radio and FIR data are not deep enough for us to reliably analyse a SFR-inclination gradient at these wavelengths, due to the potential for selection bias. However, the samples do not show any inclination trend in the upper envelope SFR (not affected by limits) probed by the surveys. Secondly, the fraction of limits to detections is approximately constant in bins of inclination. Therefore, our data are consistent with galaxies being transparent at FIR and radio wavelengths.

The FUV samples give slightly shallower slopes at $z \sim 0.7$ than at $z \sim 0$. This could be partially influenced by the flux limits of the COSMOS surveys meaning that only galaxies with relatively large SFR/SFR$_{MS}$ are detected. These limitations were not taken into account in our linear model.

The $z \sim 0$ and $z \sim 0.7$ slopes for the UV are consistent at the 1.65 sigma level. In Appendix A we show that using the SFR$_{12\mu m}$ for normalisation rather than the SFR$_{MS}$ gives fully consistent slopes of -0.6 at both redshifts. This suggests that no significant evolution has occurred in the dust properties or dust-star geometry between $z = 0$ and $z = 0.7$.

3.2. Intercept: SFR calibration and selection effects

The y-intercept represents how the SFR measured for a face-on galaxy compares to the main sequence SFR at our given redshifts and stellar mass. In absence of other effects such as foreground dust at high scale height, the y-intercept approximately represents the ratio between SFR$_\lambda$ of a face-on galaxy and the average total SFR (i.e. SFR$_{IR}$ + SFR$_{UV}$) of a MS galaxy.

The UV SFR observed is lower than the MS SFR at all given inclinations, resulting in a negative y-intercept. We find that the UV SFR under-predicts the MS SFR by ~0.74 dex at $z \sim 0.7$, compared to ~0.2 at $z \sim 0$. This implies that a larger fraction of the stellar light is attenuated and re-emitted in the infrared in the higher-redshift galaxies. We discuss this further in Sects. 3.3 and 4.

The distributions of y-intercepts for the FIR and radio wavelength subsamples, all of them positive, are dominated by sample-selection effects, in particular, the flux limit of the surveys. The radio and infrared samples lie above the MS due to

Table 3. Best-fit parameters of SFR vs. inclination where SFR is normalised by the MS SFR given the galaxy mass: median, 5th, and 95th percentile of the distribution.

λ	Slope	Intercept
SFR$_{UV}$ $z \sim 0$	$-0.79\,^{+0.08}_{-0.09}$	$-0.20\,^{+0.04}_{-0.03}$
SFR$_{MIR}$ $z \sim 0$	$-0.12\,^{+0.03}_{-0.02}$	$0.05\,^{+0.01}_{-0.01}$
SFR$_{FIR}$ $z \sim 0$	$-0.06\,^{+0.22}_{-0.20}$	$0.67\,^{+0.09}_{-0.09}$
SFR$_{radio}$ $z \sim 0$	$-0.10\,^{+0.20}_{-0.22}$	$0.52\,^{+0.11}_{-0.09}$
SFR$_{UV}$ $z \sim 0.7$	$-0.54\,^{+0.18}_{-0.17}$	$-0.74\,^{+0.08}_{-0.08}$
SFR$_{MIR}$ $z \sim 0.7$	$-0.03\,^{+0.10}_{-0.09}$	$0.28\,^{+0.05}_{-0.05}$
SFR$_{FIR}$ $z \sim 0.7$	$-0.02\,^{+0.23}_{-0.25}$	$0.54\,^{+0.15}_{-0.13}$
SFR$_{radio}$ $z \sim 0.7$	$-0.17\,^{+0.31}_{-0.33}$	$0.68\,^{+0.19}_{-0.18}$

their shallow observations not being able to detect emission from MS galaxies.

If the SFR calibrations or main-sequence relations were incorrect, we would expect this to alter the absolute offset value. However, using a "concordance" MS evolution fitted to a compilation of data (as done here) is expected to average out differences in normalisation arising due to different methods or SFR tracers. Normalising the SFR$_{UV}$ to the SFR$_{MIR}$ for galaxies detected in both UV and MIR wavelengths gave intercept values of -0.27 ± 0.03 and -1.0 ± 0.1 for the $z \sim 0$ and $z \sim 0.7$ samples (Appendix A.2). However, this result is still dependent on the accuracy of the SFR calibrations at each redshift (see Appendix B).

The MS has a scatter of ~0.3 dex (Schreiber et al. 2015), meaning that some of the scatter seen in Fig. 3 is due to the fact that galaxies might have true SFRs higher or lower than the average MS SFR used for normalisation.

3.3. Opacity at UV wavelengths: Tuffs et al. (2004) models

At UV wavelengths our observations show a clear trend of increasing attenuation with galaxy inclination and a clear evolution of the overall attenuation with redshift. Tuffs et al. (2004) calculate the attenuation of stellar light for a grid of disk opacity and inclination, providing a direct comparison to our observations.

Tuffs et al. (2004) calculated the attenuation of stellar light from local spiral galaxies using geometries that are able to reproduce observed galaxy SEDs from the UV to the submillimetre. The model predictions of Tuffs et al. (2004), which are based on the dust model of Popescu et al. (2000), are shown in Fig. 5. The model includes an exponential diffuse dust disk that follows a disk of old stars, a second diffuse dust disk that is designed to emulate the dust in spiral arms by having the same spatial distribution of the young stellar population (the thin disk), a distribution of clumpy, strongly heated grains, correlated with star-forming regions, and a dustless de Vaucouleurs bulge. The so-called clumpy dust component was required to reproduce the FIR colours and is associated with the opaque parent molecular clouds of the massive stars (Tuffs et al. 2004). The diffuse dust disk associated with the spiral arms was needed to account for the sub-millimetre emission.

Tuffs et al. (2004) have calculated attenuation curves (the change of magnitude Δm due to dust attenuation) of the thin disk, thick disk, and bulge component (Δm vs. $1 - \cos(i)$) and
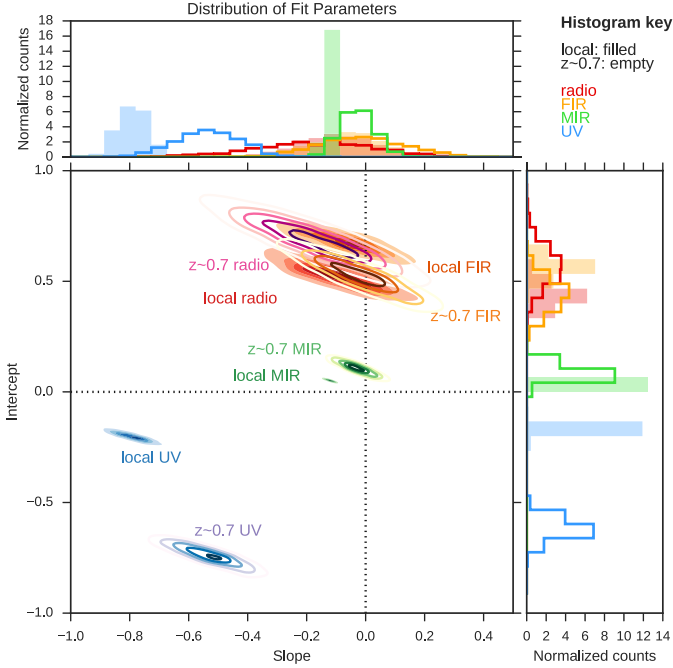
Fig. 4. Joint and marginalised distributions of the linear model parameters fit to the data shown in Fig. 3. Filled histograms correspond to SDSS-based samples and the open histograms correspond to COSMOS-based samples. Distributions for the slope and the intercept are shown with histograms normalised so that they encompass an area of 1. The median of each parameter distribution is given in Table 3.

they have been represented with a fifth-order polynomial at various τ_B^f and wavelengths, where τ_B^f is the opacity through the centre of a face-on galaxy in the B-band. Since τ_B^f is the opacity through the centre of the galaxy where most of the dust is concentrated, $\tau_B^f \gtrsim 1.0$ corresponds to an optically thin galaxy over most of its area. The attenuation calculations in the UV range were only performed on the thin disk because the thick disk is assumed not to emit in the UV.

We linearly interpolated the relation for UV attenuation at 1350 and 1650 Å, tabulated in Tuffs et al. (2004) for B-band opacities of $\tau_B^f = 0.5, 1.0, 2.0, 4.0,$ and 8.0 to obtain the expected UV attenuation at 1542 Å, the effective wavelength of the GALEX FUV filter. We show how the expected UV attenuation affects the SFR$_{UV}$ using the tabulated relation at B-band opacities of $\tau_B^f = 0.5, 1.0, 2.0, 4.0,$ and 8.0 in Fig. 5.

The attenuation by the clumpy dust component is independent of the inclination of the galaxy, unlike the diffuse dust component. The clumpy dust component is associated with opaque parent clouds of massive stars; no UV light will escape the cloud independent of the viewing angle. The wavelength dependence of the attenuation is also not determined by the optical properties of the grains because the clouds are opaque at each wavelength. Instead, wavelength dependence arises because stars migrate away from their birth cloud over time, and therefore lower-mass, redder stars are more likely to have left their birth clouds and thus their starlight will be less attenuated (Tuffs et al. 2004). The Tuffs et al. (2004) models analytically treat the attenuation due to the clumpy component separately, parametrized by the mass fraction of dust in the clumpy component, F.

Assuming that only the thin disk emits in the UV range and the disk and bulge only in the optical/NIR range as suggested by Tuffs et al. (2004), we can vary the fraction of the emitted FUV

flux density, F_{FUV}, that is locally absorbed in the star-forming regions by the clumpy dust component. The total attenuation would then be

$$\Delta m_{UV} = \Delta m_{UV}^{tdisk} - 2.5 \log (1 - F_{FUV}), \qquad (6)$$

where Δm_{UV}^{tdisk} is the thin disk attenuation given in Tuffs et al. (2004) and $F_{FUV} = f_{FUV} \times F$, where F is the clumpiness fraction and $f_{FUV} = 1.36$ at 1542 Å (the wavelength dependence of the probability that a UV photon will be completely absorbed locally). In this way F will change the overall normalisation of the SFR$_{UV}$ inclination relation.

We use the Goodman-Weare Monte Carlo Markov chain (MCMC) sampling method implemented in the *python* package *emcee.py* (Foreman-Mackey et al. 2013) to find posterior distributions of τ_B^f and F for our local UV galaxy sample. We use an uninformative flat prior between $\tau_B^f = [0, 10]$ and $F = [0, 0.61]$. The maximum $F = 0.61$ constraint corresponds to the case where there is a complete lack of cloud fragmentation due to feedback and the probability that photons will escape into the diffuse ISM is determined only by the migration of stars away from their birth-clouds (Popescu et al. 2011). We keep 800 steps (after a 200 step burn-in) from 50 MCMC walkers. The posterior median values of parameters with 68% credible intervals for the Tuffs et al. (2004) models at $z \sim 0$ are $\tau_B^f = 3.95^{+0.16}_{-0.15}$ and $F = 0.09^{+0.02}_{-0.02}$. In Fig. 5, we show in green 100 samples drawn randomly from the chain.

The attenuation curves for models with τ_B^f ranging from 0.5 (light grey) to 8 (dark grey) and $F = 0.22$ are also shown with our data in Fig. 5. Tuffs et al. (2004) suggested using $F = 0.22$ because it was the median value obtained from fitting five nearby edge-on spirals, and that value was also obtained for the prototype galaxy NGC 891. On the other hand, Popescu et al. (2011) find a clumpiness fraction of $F = 0.41$ for typical spiral galaxies in the local universe. Using the FUV, which is most sensitive to the clumpiness factor, we find lower values for F in local galaxies than Tuffs et al. (2004) and Popescu et al. (2011). However, we are insensitive to dust clouds that are completely obscured in the FUV but still radiate in the infrared. This is likely the reason why the clumpiness factors we measure for the FUV are lower than the SED results that include infrared emission (by a factor of ~2).

Driver et al. (2007) found $\tau_B^f \sim 3.8 \pm 0.7$, derived from integrated galaxy properties of ~10 000 galaxies with bulge-disk decompositions, consistent with our result at $z \sim 0$. At this face-on central optical depth, less than half the bolometric luminosity is actually absorbed by dust (Tuffs et al. 2004).

For the $z \sim 0.7$ sample, we noticed that the fits were dominated by the high-S/N data points with high SFRs, giving preferentially shallower slopes. The S/N effects are more important at $z \sim 0.7$ because the detection threshold is close to the data (as opposed to $z \sim 0$, where the detection threshold is well below our data). Ignoring the errors on the SFR by setting them all to a constant 0.3 dex, and considering only galaxies with $1 - \cos(i) < 0.75$, where we are more complete in sSFR, we obtain $\tau_B^f = 3.5^{+1.1}_{-1.8}$ and $F = 0.55^{+0.06}_{-0.04}$. Including all data points gives a smaller $\tau_B^f = 2.0^{+0.5}_{-0.3}$ and a correspondingly larger $F = 0.60^{+0.01}_{-0.02}$.

The spread in attenuations in both samples could also be partially explained by the fact that galaxies have different clumpy dust fractions. Misiriotis et al. (2001) found that F varies by 30% between galaxies.
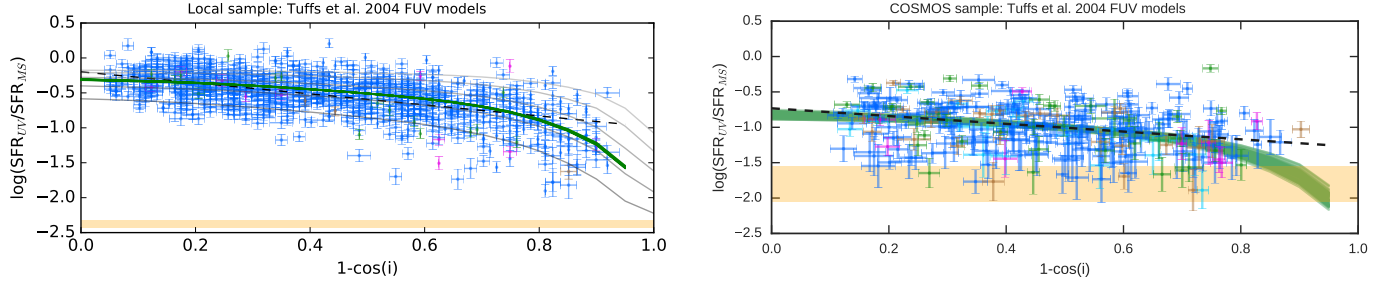
Fig. 5. SFR_{UV}-inclination relation shown in the top panels of Fig. 3, but with the attenuation curves of Tuffs et al. (2004) showing the expected change in flux, and hence SFR_{UV}, with inclination. Green trends show the relations that best fit our data, with $\tau_B^f = 3.95^{+0.16}_{-0.15}$ and $F = 0.09^{+0.02}_{-0.02}$ for the local sample (*left*) and $\tau_B^f = 3.5^{+1.1}_{-1.8}$, $F = 0.55^{+0.06}_{-0.04}$ for the COSMOS sample (*right*). In the *left panel*, models shown have face-on B-band opacities of $\tau_B^f = 0.5, 1.0, 2.0, 4.0,$ and 8.0 (from light to dark grey) and $F = 0.22$.

In this analysis, τ_B^f decreases with redshift while F increases, meaning the overall opacity increases as it is dominated by F at UV wavelengths. The decrease in τ_B^f is in apparent contradiction with the Sargent et al. (2010) result that reported more opaque galaxies at $z = 0.7$ in the B band. However, we note that the errors on τ_B^f are so large that the decrease reported in this analysis is not statistically significant. Furthermore, we find that normalising the SFR_{UV} by a different MS produces an increase in τ_B^f with redshift, while changing the normalisation did not change the fact that F increases between $z \sim 0$ and $z \sim 0.7$, a key result which we discuss in Sect. 4.

3.4. UV opacity and stellar mass surface density

Grootes et al. (2013) found that the opacity of spiral galaxies in the local Universe ($z \leq 0.13$) depends on the stellar mass surface density μ_*. De Vis et al. (2017) also report a mass surface density dependence of the B-band opacity and suggest that the increased stellar mass potential associated with higher stellar mass surface density creates instabilities in the cold ISM, which lead to the formation of a thin dust disk that increases the attenuation (Dalcanton et al. 2004). Williams et al. (2010) show that the stellar mass surface density increases with redshift out to $z \sim 2$. We re-compute our SFR_{FUV}-inclination relations in bins of μ_* to investigate this dependence. We compute μ_* for each galaxy using the stellar mass and the physical half-light radius from the rest-frame g band GIM2D fits,

$$\mu_* = \frac{M_*}{2r_{1/2}^2}. \tag{7}$$

Figure 6 shows the distribution of $\log(\mu_*)$ for our samples at $z \sim 0$ and $z \sim 0.7$. We note that μ_* was calculated with the original stellar mass and half-light radius values, without any inclination corrections. Before slicing the samples into bins of μ_*, we corrected $\log(\mu_*)$ for inclination dependence as done in Sect. 2.3.

Figure 6 shows that in the local Universe, the slope of the SFR_{FUV}-the inclination is steeper for galaxies with higher μ_* when considering our sample of large and massive galaxies. This supports the trend reported in Grootes et al. (2013) that opacity is proportional to μ_*. At $z \sim 0.7$, no trend between slope and μ_* is discernible within the scatter (some bins have scatters smaller than the symbol size). On the other hand, the intercept of the SFR_{FUV}-inclination relation (the attenuation of face-on disks), clearly decreases (increases) with μ_* for the COSMOS samples.
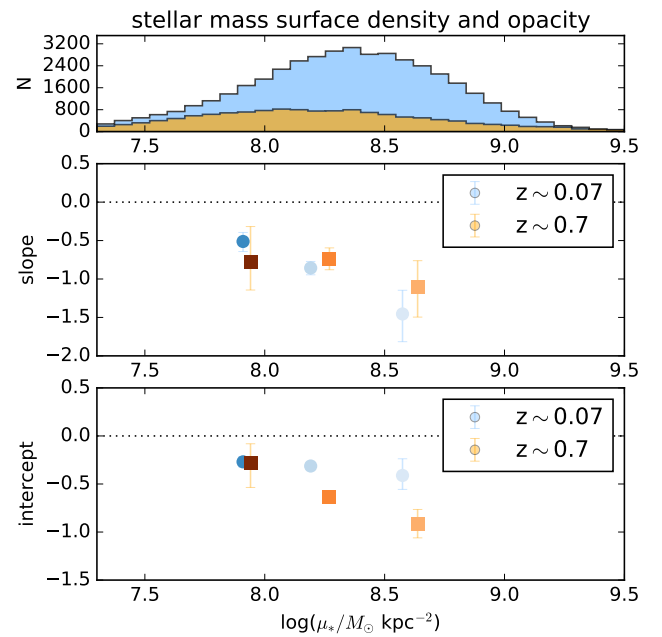

Fig. 6. *Top panel*: distribution of stellar mass surface densities, μ_*, for our two redshift ranges. *Middle panel*: relation between opacity, represented by the slope of the SFR_{FUV}-inclination relation, and stellar mass surface density. *Bottom panel*: relation between overall UV attenuation, represented by the intercept of the SFR_{FUV}-inclination relation, and μ_*. Data are colour-coded by the median size, $r_{1/2}$, of each bin in the *bottom panel*, with colours ranging from 4 kpc (light) to 7 kpc (dark).

Grootes et al. (2013) constrained τ_B^f using the FIR SED to measure the dust mass while keeping the clumpiness factor fixed at $F = 0.41$. We might expect that the IR-derived τ_B^f of Grootes et al. (2013) should be more closely related to our values for the intercept of the SFR_{FUV}-inclination relation. For the total attenuation corrections, both the slope and the intercept are important.

We also find that the slope of the SFR_{UV}-inclination relation becomes steeper at higher stellar masses at both $z \sim 0$ and $z \sim 0.7$ (not shown). This indicates that the most massive galaxies are more opaque, and their SFRs are most affected by galaxy inclination.

4. Evolution of disk opacity

Ultra-violet observations are sensitive to dust attenuation, showing trends that other wavelengths do not, allowing us to probe disk opacity. We study the UV-derived SFR of disk-dominated
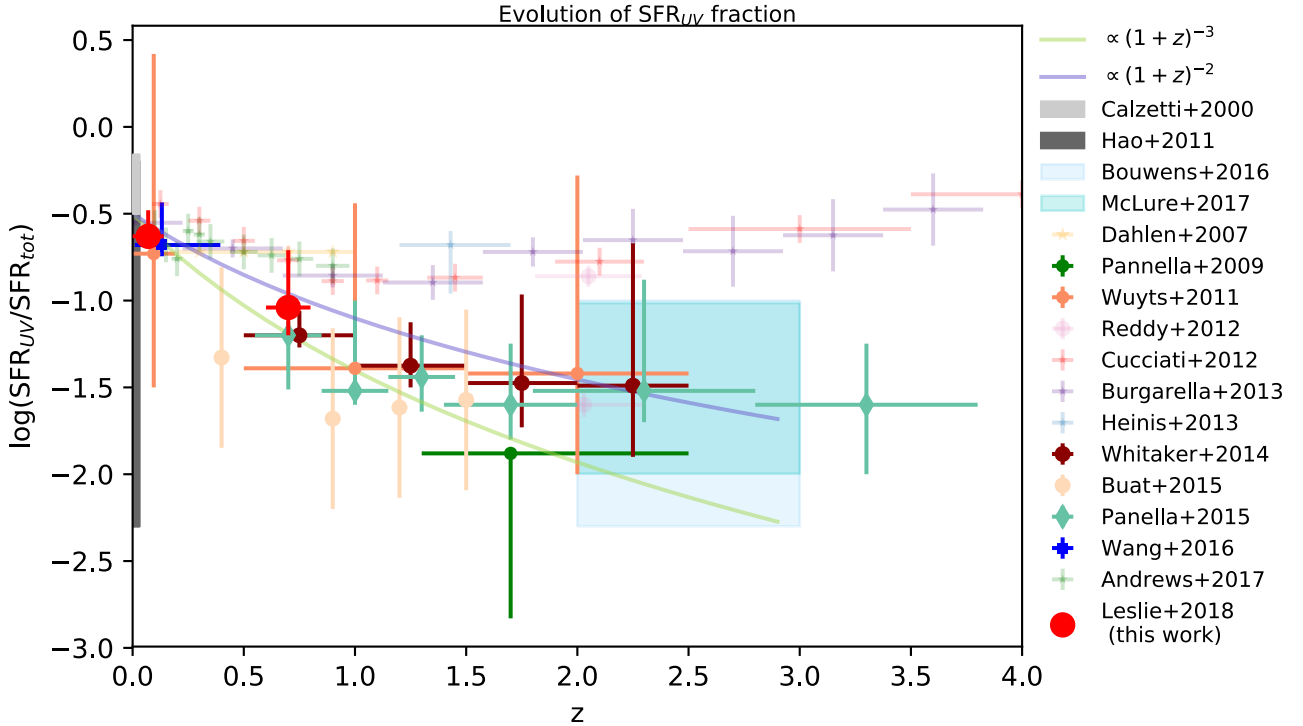
Fig. 7. Evolution of SFR_{UV}/SFR_{tot} for statistical samples of galaxies at $z < 4$. SFR_{tot} is the sum of the attenuated (SFR_{IR}) and non-attenuated (SFR_{UV}) emission. Studies that included mass-dependent measurements are Wuyts et al. (2011b), Pannella et al. (2009, 2015), Whitaker et al. (2014), McLure et al. (2018), and Bouwens et al. (2016). For these studies, the error-bars show the range of SFR_{UV}/SFR_{tot} for galaxies with stellar masses $10.2 < \log(M_*/M_\odot) < 11.4$, to match the sample of massive galaxies used in this work. Bouwens et al. (2016) and McLure et al. (2018) combined literature results and are shown as shaded areas. Studies that include less-massive galaxies (shown with transparent symbols) have, on average, less attenuated UV emission, so the SFR_{UV}/SFR_{tot} ratio is higher. The red dots show the value of SFR_{UV}/SFR_{MS} we obtained for a disk galaxy inclined at $1 - \cos(i) = 0.5$ ($i = 60\,\mathrm{deg}$). More information about the studies included in this figure is provided in Appendix C. To convert the y-axis to A_{FUV} we multiply by -2.5. Two solid lines show evolution of SFR_{UV}/SFR_{tot} between $(1 + z)^{-2}$ (purple) and $(1 + z)^{-3}$ (lime green) normalised to -0.5 at $z = 0$. The evolution of FUV attenuation for massive galaxies evolves as $(1 + z)^{2-3}$ up to $z \sim 2$.

galaxies at $z \sim 0$ and $z \sim 0.7$ and find a strong inclination dependence that appears to be redshift independent. We infer that the overall FUV attenuation has increased between $z \sim 0$ and $z \sim 0.7$ from the collective decreased fraction of SFR_{UV}/SFR_{MS} ratios. To try to understand how the combination of (a) a largely unchanging slope of the UV attenuation–inclination relation, and (b) an evolving overall attenuation might arise we employ the Tuffs et al. (2004) models. We find that an increased dust clumpiness can explain most of the increase in attenuation while keeping the slope consistent.

In the models of Tuffs et al. (2004), the FUV emission and the clumpy dust component surrounding the HII regions are assumed to only be associated with the thin disk. The fraction of dust mass in the clumpy component is parametrized by F and we find best fitting values $F = 0.09^{+0.02}_{-0.02}$ and $F = 0.55^{+0.06}_{-0.04}$ for the $z \sim 0$ and $z \sim 0.7$ samples, respectively. We find that the fraction of SFR that is attenuated increases by a factor of ~ 3.4 for face-on galaxies, which corresponds to the increase in the viewing-angle-independent clumpy dust fraction F by a factor of ~ 6 from $z = 0.07$ to $z = 0.7$. We also find that the average face-on B-band opacity, τ_f^B, does not evolve strongly with redshift when traced by the FUV emission ($\Delta \tau_B^f = -0.45^{+1.1}_{-1.8}$; consistent with zero). At $z \sim 0.7$, galaxies at fixed stellar mass had more mass in gas, and therefore higher SFRs, by factors of ~ 3–4. Stars are born from the dusty molecular clouds and the young stars then heat the dust that is encompassing them; the warm clumpy component thus somewhat traces the recent star formation. An increased clumpy-dust fraction should change the shape of the infrared SED with redshift. Indeed, many studies

find that the peaks of the IR SEDs move to shorter rest frame wavelengths with redshift (implying a warmer component in the FIR emission, e.g. Magnelli et al. 2014; Béthermin et al. 2015).

The star and dust geometry are crucial to understanding how galaxy properties such as observed size $r_{1/2}$ or UV attenuation are affected by dust attenuation. We note that the geometry of the Tuffs et al. (2004) model may not be valid at $z > 0$. We caution that measuring the slope or normalisation of the SFR_{FUV}-inclination equation alone does not give a full picture of the dust. For example, a lack of slope could be because a large amount of dust at large scale heights heavily absorbs light even when the galaxy is face-on. Therefore, the slope and the intercept should be considered together for a better understanding of the dust content. Gas disks are observed to become puffier at higher redshift, having larger scale heights perhaps due to a larger gas fraction and turbulence (e.g. Kassin et al. 2012; Förster Schreiber et al. 2009; Wisnioski et al. 2015). If the stellar disk height also increases with redshift, then the minimum axis ratio used in calculating inclination (Eq. (2)) must be adjusted accordingly. To date, no studies have conclusively measured the scale height of stellar disks as a function of redshift. However, we find no significant difference in the minimum observed axis ratio of our two samples (see Fig. 1), suggesting that the stellar disk height has not increased significantly by $z = 0.7$. The Tuffs et al. (2004) model assumption of the thick disk not emitting at UV wavelengths might still be a valid assumption at $z \sim 0.7$. A comparison to simulations that include different dust components, such as those presented recently by Nelson et al. (2018), or other hydrodynamical and radiative transfer simulations such

as Jonsson et al. (2010) or Trayford et al. (2017), should allow us to test our assumptions about the relative stellar and dust geometries at $z \sim 0.7$ and verify whether an increase of the clumpy dust-component is responsible for the increase of the FUV attenuation of massive galaxies with redshift.

In Fig. 7, we compare the FUV attenuation as represented by SFR_{UV}/SFR_{tot} for our two redshift bins with other studies from the literature. We find a large variation in SFR_{UV}/SFR_{tot} when considering galaxies drawn from different studies that have different sample selections. Our findings cannot be extrapolated to the general galaxy population. Studies that include less massive galaxies (represented by symbols with higher transparency) tend to show larger SFR_{UV}/SFR_{tot} ratios, that is, less UV attenuation than samples restricted to more massive galaxies ($\log(M_*/M_\odot) > 10.2$). Studies at redshifts $z > 1.5$, such as Pannella et al. (2015) and McLure et al. (2018), find that stellar mass provides a better prediction of UV attenuation than β, the UV slope itself. Wuyts et al. (2011b) compared their observed SFR_{UV}/SFR_{IR} with what would be expected from the SFR surface density, assuming a simple model with a homogeneously mixed star-gas geometry. They found that more NUV (2800 Å) emission escaped than expected from the simple model at $z > 1$, which they suggest could be due to a more patchy geometry in high-redshift galaxies. For more information about the data included in Fig. 7, please refer to Appendix C.

We find that the overall FUV attenuation increases with redshift for large, massive star-forming galaxies. Interstellar dust is produced in stars which in turn form from the gas; the fact that the dust- and gas-mass fractions vary similarly with redshift is a good consistency check, displayed in Fig. 8. However, the amount of total dust depends on the balance between dust creation and destruction. Keeping track of the interstellar dust that is produced in the ejecta of asymptotic giant branch (AGB) stars and supernovae, the growth of dust grains in dense regions of the ISM, and the destruction of dust in supernovae shocks and collisions is, nevertheless, a difficult task (e.g. Aoyama et al. 2017; Popping et al. 2017). If we assume, simply, that the increased dust mass with redshift all goes into the clumpy dust component, and that the clumpy component is related to the molecular gas (in terms of amount and distribution) then the amount of overall attenuation could follow the evolution in molecular gas mass. Figure 8 shows that the FUV attenuation does not evolve as strongly as the gas mass fraction (as found recently by Whitaker et al. (2017) out to $z \sim 2.5$; however, the fraction of dust in the clumpy component (F) does evolve strongly with redshift, similar to the gas-mass fraction.

da Cunha et al. (2010), Smith et al. (2012), Sandstrom et al. (2013), and Rowlands et al. (2014) found that, in the local Universe, M_d/M_* is proportional to sSFR. Studies such as Sargent et al. (2012) and Tasca et al. (2015), that look at how sSFR changes with redshift, find that the sSFR varies as $sSFR \propto (1 + z)^{2.8}$ out to redshifts $z < 2$. This would give a sSFR increase by a factor of ~ 3.6 between $z = 0.07$ and $z = 0.7$. We note, however, that this trend also is stellar mass dependent (e.g. Schreiber et al. 2015), and that lower-mass galaxies have a shallower evolution in sSFR than the most massive galaxies.

Recent studies of molecular gas at high redshifts indicate that the cosmic density of molecular gas, similar to the cosmic density of star formation, peaks between redshifts 2 and 3 (Decarli et al. 2016). Genzel et al. (2015), Sargent et al. (2014), and Tacconi et al. (2018) used compilations of studies that measure gas mass via CO line luminosities and found that M_g/M_* varies like $(1 + z)^{2.7}$, which corresponds to an increase by a factor of ~ 3.5 between $z = 0.07$ and $z = 0.7$. On the other
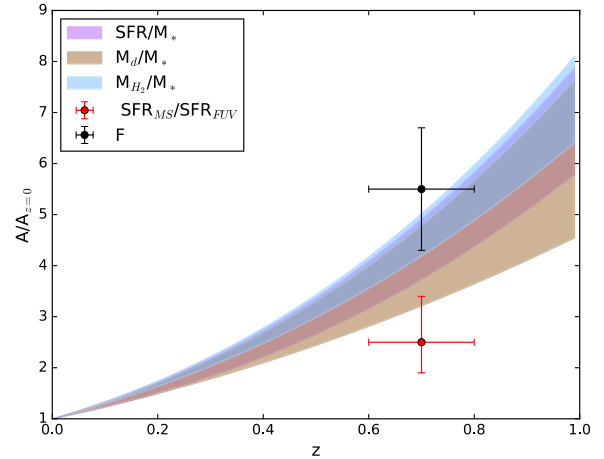

Fig. 8. Evolution of massive galaxy properties from their local values out to $z \sim 1$. The evolution of the dust-mass fraction (M_d/M_*) was determined from a power-law fit to data from Santini et al. (2014), Béthermin et al. (2015) (for $z \leq 1$), and Rémy-Ruyer et al. (2014) for $z = 0$. The upper bound to the M_d/M_* evolution is given by assuming $M_d \sim 0.5 \times Z \times M_g$, and the evolution of gas and metallicity over this redshift and stellar mass range. The evolution of specific SFR is shaded purple between the relationship in Sargent et al. (2014) and $(1 + z)^3$. The evolution of the molecular gas fraction (blue) is from Tacconi et al. (2018). We find that the fraction (F) of dust in clumps surrounding nascent star-forming regions has increased by a factor of ~ 5.5, and that the overall attenuation of UV (SFR_{MS}/SFR_{UV}) has increased by a factor of ~ 2.5 (ranging from 3.4 to 1.9 for face-on to edge-on galaxies, respectively).

hand, Bauermeister et al. (2013) expect $M_g/M_* \propto (1 + z)^{3.2}$ which would imply an increase in the gas mass fraction by a factor of ~ 4.4. In any case, the gas mass is expected to increase by a factor of ~ 4 between our two redshift slices. In Fig. 7, we show with two solid lines the relations $SFR_{UV}/SFR_{tot} \propto (1 + z)^{-2}$ and $\propto (1 + z)^{-3}$.

The parameter that most strongly controls the dust-to-gas mass is the metallicity (e.g. Leroy et al. 2011; Accurso et al. 2017). According to the parametrization of Zahid et al. (2014), a galaxy with $\log(M_*/M_\odot) = 10.2$ would have a metallicity of 0.069 dex less at $z = 0.7$ than at $z = 0.07$. A galaxy at $M_* \sim 10^{10.5} M_\odot$, on the other hand, will have a change in metallicity of 0.035 dex between the same two redshifts. For our sample, the dust to gas ratio should not change significantly between $z \sim 0$ and $z \sim 0.7$, however, we take this change into account in Fig. 8 when calculating the expected M_d/M_* evolution based on the dust-to-gas ratio.

To summarise, out to $z < 2$, sSFRs increase as $(1 + z)^{2.8}$ and M_g/M_* and M_d/M_* increase at a similar rate for galaxies more massive than $10^{10} M_\odot$ (Santini et al. 2014). Since $z = 0.7$, SFRs and gas and dust masses have decreased by factors of ~ 3.5. We see a larger systematic FUV attenuation in the $z \sim 0.7$ sample compared to the $z \sim 0$ sample. The SFR_{FUV} of a face-on galaxy lies ~ 0.21 dex below the MS at $z = 0.07$, and ~ 0.74 dex below the MS at $z = 0.7$. Assuming the main-sequence SFR to be the unobscured SFR, or $SFR_{UV} + SFR_{IR}$, the FUV attenuation of face-on galaxies has thus increased by a factor of ~ 3.4.

Galaxies are thought to grow in size over time ("inside-out growth"). For example, Wuyts et al. (2011b) shows that galaxies on the main sequence at a fixed stellar mass have a larger size on average at $z \sim 0.1$ than at $z \sim 1$. Due to this evolution, and the fact that opacity also varies with radius in galaxies out to at least $z < 2$ (Tacchella et al. 2018; Wang et al. 2017), we cannot interpret the slopes of the attenuation–inclination

relation reported in this paper in the context of an evolutionary picture for particular galaxies. Instead, we emphasise that the inclination dependence of the UV attenuation in the largest and most massive star-forming disk galaxies at $z \sim 0.7$ (which are not necessarily the same galaxies that will end up in our sample at $z = 0.07$), behaves similarly to that in galaxies selected to have the same stellar mass and radius at $z \sim 0$. However, the overall FUV attenuation has increased, presumably due to the larger amount of dust at higher redshifts.

The importance of inclination-dependent FUV SFRs, even when common attenuation corrections have been applied, will be the subject of Paper II.

5. Conclusions

We parametrize the attenuation of starlight as a function of galaxy disk inclination to investigate the global dust properties by fitting a simple linear function to the SFR-inclination relation for a sample of galaxies at $z \sim 0$ (in SDSS) and $z \sim 0.7$ (in COSMOS). We compiled two samples of galaxies at four different wavelengths: FUV, MIR (12 μm), FIR (60 μm) and radio (20 cm) with well measured optical morphology for which we calculated monochromatic SFRs. Our findings can be summarised as follows. Massive disks ($\log(M_*/M_\odot) > 10.2$) larger than 4 kpc, show strong FUV SFR-inclination trends at both $z \sim 0$ and $z \sim 0.7$. Our fit to this relation is sensitive to selection effects, in particular, to flux limits and size cuts. The FUV SFR of face-on galaxies at $z \sim 0.7$ is less than that expected from the main-sequence relation by a factor of 0.74 ± 0.09 dex, compared to 0.20 ± 0.03 dex at $z \sim 0$. This corresponds to an increase of the FUV attenuation of face-on galaxies by a factor ~ 3.4 over the last 7.5 Gyr. An increased fraction of dust in warm clumpy components surrounding the HII regions (by a factor of about 6) could explain this increased overall attenuation while simultaneously allowing the opacities (the slope) to remain constant. This increase in the warm clump component and UV attenuation between $z \sim 0$ and $z \sim 0.7$ is consistent with the increased molecular gas content in galaxies at redshift 0.7. Overall FUV attenuation increases with stellar mass surface density at both $z \sim 0$ and $z \sim 0.7$. It is likely that no opacity is present in the FIR and radio, however, we were unable to confirm this for our FIR and radio subsamples as our data did not span a sufficient range in luminosity due to survey flux limits. MIR and radio SFRs are inclination independent and therefore MIR and radio data can provide a useful tracer of SFRs also for galaxies with a high inclination angle.

The increase in FUV attenuation for massive galaxies follows the amount of evolution in SFR, gas, and dust mass fractions over the past 7.5 billion years. These phases (gas, dust and star formation) are therefore closely related, probably even spatially related; an assumption which is used for deriving gas masses from dust continuum emission and for energy balancing SED codes that assume the dust emission and star formation come from similar regions.

References

Abazajian, K. N., Adelman-McCarthy, J. K., Agüeros, M. A., et al. 2009, ApJS, 182, 543
Accurso, G., Saintonge, A., Catinella, B., et al. 2017, MNRAS, 470, 4750
Adelman-McCarthy, J. K. 2008, VizieR Online Data Catalog: II/282
Allen, C. W. 1976, Astrophysical Quantities (London: Athlone) 3rd edn.
Álvarez-Márquez, J., Burgarella, D., Heinis, S., et al. 2016, A&A, 587, A122
Aoyama, S., Hou, K.-C., Shimizu, I., et al. 2017, MNRAS, 466, 105
Arnouts, S., Moscardini, L., Vanzella, E., et al. 2002, MNRAS, 329, 355
Astropy Collaboration, Robitaille, T.-P., Tollerud, E.-J., et al. 2013, A&A, 558, A33
Battisti, A. J., Calzetti, D., Johnson, B. D., & Elbaz, D. 2015, ApJ, 800, 143
Bauermeister, A., Blitz, L., Bolatto, A., et al. 2013, ApJ, 768, 132
Becker, R. H., White, R. L., & Helfand, D. J. 1995, ApJ, 450, 559
Beichman, C. A., Neugebauer, G., Habing, H. J., Clegg, P. E., & Chester, T. J. 1988, in Infrared astronomical satellite (IRAS) catalogs and atlases, eds. C. A. Beichman, G. Neugebauer, H. J. Habing, P. E. Clegg, & T. J. Chester, Explanatory supplement, 1
Bendo, G. J., Wilson, C. D., Pohlen, M., et al. 2010, A&A, 518, L65
Bendo, G. J., Boselli, A., Dariush, A., et al. 2012, MNRAS, 419, 1833
Béthermin, M., Daddi, E., Magdis, G., et al. 2015, A&A, 573, A113
Bianchi, L., Efremova, B., Herald, J., et al. 2011, MNRAS, 411, 2770
Blanton, M. R., Schlegel, D. J., Strauss, M. A., et al. 2005, AJ, 129, 2562
Boissier, S., Boselli, A., Buat, V., Donas, J., & Milliard, B. 2004, A&A, 424, 465
Boissier, S., Gil de Paz, A., Boselli, A., et al. 2007, ApJS, 173, 524
Bolzonella, M., Miralles, J.-M., & Pelló, R. 2000, A&A, 363, 476
Boquien, M., Calzetti, D., Combes, F., et al. 2011, AJ, 142, 111
Bouwens, R. J., Aravena, M., Decarli, R., et al. 2016, ApJ, 833, 72
Brinchmann, J., Charlot, S., White, S. D. M., et al. 2004, MNRAS, 351, 1151
Brusa, M., Civano, F., Comastri, A., et al. 2010, ApJ, 716, 348
Bruzual, G., & Charlot, S. 2003, MNRAS, 344, 1000
Buat, V., & Xu, C. 1996, A&A, 306, 61
Buat, V., Oi, N., Heinis, S., et al. 2015, A&A, 577, A141
Burgarella, D., Buat, V., Gruppioni, C., et al. 2013, A&A, 554, A70
Calzetti, D., Armus, L., Bohlin, R. C., et al. 2000, ApJ, 533, 682
Capak, P., Aussel, H., Ajiki, M., et al. 2007, ApJS, 172, 99
Cappelluti, N., Hasinger, G., Brusa, M., et al. 2007, ApJS, 172, 341
Chabrier, G. 2003, PASP, 115, 763
Chang, Y.-Y., van der Wel, A., da Cunha, E., & Rix, H.-W. 2015, ApJS, 219, 8
Charlot, S., & Fall, S. M. 2000, ApJ, 539, 718
Chevallard, J., Charlot, S., Wandelt, B., & Wild, V. 2013, MNRAS, 432, 2061
Ciesla, L., Boselli, A., Smith, M. W. L., et al. 2012, A&A, 543, A161
Ciesla, L., Boquien, M., Boselli, A., et al. 2014, A&A, 565, A128
Cluver, M. E., Jarrett, T. H., Hopkins, A. M., et al. 2014, ApJ, 782, 90
Condon, J. J., Cotton, W. D., Greisen, E. W., et al. 1998, AJ, 115, 1693
Conroy, C., Schiminovich, D., & Blanton, M. R. 2010, ApJ, 718, 184
Cucciati, O., Tresse, L., Ilbert, O., et al. 2012, A&A, 539, A31
da Cunha, E., Charlot, S., & Elbaz, D. 2008, MNRAS, 388, 1595
da Cunha, E., Eminian, C., Charlot, S., & Blaizot, J. 2010, MNRAS, 403, 1894
Dahlen, T., Mobasher, B., Dickinson, M., et al. 2007, ApJ, 654, 172
Dalcanton, J. J., Yoachim, P., & Bernstein, R. A. 2004, ApJ, 608, 189
Dale, D. A., & Helou, G. 2002, ApJ, 576, 159
Dale, D. A., Gil de Paz, A., Gordon, K. D., et al. 2007, ApJ, 655, 863
Davies, J. I., Phillips, S., Boyce, P. J., & Disney, M. J. 1993, MNRAS, 260, 491
Davies, L. J. M., Huynh, M. T., Hopkins, A. M., et al. 2017, MNRAS, 466, 2312
Decarli, R., Walter, F., Aravena, M., et al. 2016, ApJ, 833, 69
De Geyter, G., Baes, M., Camps, P., et al. 2014, MNRAS, 441, 869
De Vis, P., Dunne, L., Maddox, S., et al. 2017, MNRAS, 464, 4680
Devour, B. M., & Bell, E. F. 2016, MNRAS, 459, 2054
Disney, M., Davies, J., & Phillipps, S. 1989, MNRAS, 239, 939
Donley, J. L., Koekemoer, A. M., Brusa, M., et al. 2012, ApJ, 748, 142
Draine, B. T., & Li, A. 2007, ApJ, 657, 810
Draine, B. T., Dale, D. A., Bendo, G., et al. 2007, ApJ, 663, 866
Driver, S. P., Popescu, C. C., Tuffs, R. J., et al. 2007, MNRAS, 379, 1022
Driver, S. P., Hill, D. T., Kelvin, L. S., et al. 2011, MNRAS, 413, 971
Foreman-Mackey, D., Hogg, D. W., Lang, D., & Goodman, J. 2013, PASP, 125, 306

Förster Schreiber, N. M., Genzel, R., Bouché, N., et al. 2009, ApJ, 706, 1364
Galliano, F., Hony, S., Bernard, J.-P., et al. 2011, A&A, 536, A88
Genzel, R., Tacconi, L. J., Lutz, D., et al. 2015, ApJ, 800, 20
Giovanelli, R., Haynes, M. P., Salzer, J. J., et al. 1994, AJ, 107, 2036
Giovanelli, R., Haynes, M. P., Salzer, J. J., et al. 1995, AJ, 110, 1059
González, R. A., Allen, R. J., Dirsch, B., et al. 1998, ApJ, 506, 152
Grootes, M. W., Tuffs, R. J., Popescu, C. C., et al. 2013, ApJ, 766, 59
Guthrie, B. N. G. 1992, A&AS, 93, 255
Hao, C.-N., Kennicutt, R. C., Johnson, B. D., et al. 2011, ApJ, 741, 124
Hasinger, G., Cappelluti, N., Brunner, H., et al. 2007, ApJS, 172, 29
Heinis, S., Buat, V., Béthermin, M., et al. 2013, MNRAS, 429, 1113
Holmberg, E. 1958, Meddelanden fran Lunds Astronomiska Observatorium
    Serie II, 136, 1
Holmberg, E. 1975, Magnitudes, Colors, Surface Brightness, Intensity Distri-
    butions Absolute Luminosities, and Diameters of Galaxies, ed. A. Sandage,
    M. Sandage, & J. Kristian (The University of Chicago Press), 123
Holwerda, B. W., Gonzalez, R. A., Allen, R. J., & van der Kruit, P. C. 2005, AJ,
    129, 1396
Hubble, E. P. 1926, ApJ, 64, 321
Huber, P. J. 1981, Robust statistics Wiley Series in Probability and Mathematical
    Statistics (New York: Wiley), 1981
Huizinga, J. E., & van Albada T. S. 1992, MNRAS, 254, 677
Hunt, L. K., Draine, B. T., Bianchi, S., et al. 2015, A&A, 576, A33
Hunter, J. D. 2007, Matplotlib: A 2D Graphics Environment, Computing in
    Science & Engineering, 9, 90
Ilbert, O., Arnouts, S., McCracken, H. J., et al. 2006, A&A, 457, 841
Ilbert, O., McCracken, H. J., Le Fèvre, O., et al. 2013, A&A, 556, A55
Ilbert, O., Arnouts, S., Le Floc'h, E., et al. 2015, A&A, 579, A2
Ivezić, Ž., Menou, K., Knapp, G. R., et al. 2002, AJ, 124, 2364
Jones, A. P., Tielens, A. G. G. M., & Hollenbach, D. J. 1996, ApJ, 469, 740
Jones, A. P., Fanciullo, L., Köhler, M., et al. 2013, A&A, 558, A62
Jonsson, P., Groves, B. A., & Cox, T. J. 2010, MNRAS, 403, 17
Kampczyk, P., Lilly, S. J., Carollo, C. M., et al. 2007, ApJS, 172, 329
Karim, A., Schinnerer, E., Martínez-Sansigre, A., et al. 2011, ApJ, 730, 61
Kassin, S. A., Weiner, B. J., Faber, S. M., et al. 2012, ApJ, 758, 106
Kauffmann, G., Heckman, T. M., Tremonti, C., et al. 2003, MNRAS, 346, 1055
Keel, W. C., & White, III, R. E. 2001, AJ, 121, 1442
Kennicutt, R. C., & Evans, N. J. 2012, ARA&A, 50, 531
Kennicutt, Jr. R. C., Armus, L., Bendo, G., et al. 2003, PASP, 115, 928
Kewley, L. J., Jansen, R. A., & Geller, M. J. 2005, PASP, 117, 227
Kewley, L. J., Groves, B., Kauffmann, G., & Heckman, T. 2006, MNRAS, 372,
    961
Kimball, A. E., & Ivezić, Ž. 2008, AJ, 136, 684
Kimball, A., & Ivezić, Z. 2014, ArXiv e-prints [arXiv: 1401.1535]
Koekemoer, A. M., Aussel, H., Calzetti, D., et al. 2007, ApJS, 172, 196
Kroupa, P. 2001, MNRAS, 322, 231
Laigle, C., McCracken, H. J., Ilbert, O., et al. 2016, ApJS, 224, 24
Lang, P., Wuyts, S., Somerville, R. S., et al. 2014, ApJ, 788, 11
Larson, D., Dunkley, J., Hinshaw, G., et al. 2011, ApJS, 192, 16
Lee, J. C., Hwang, H. S., & Ko, J. 2013, ApJ, 774, 62
Lee, N., Sanders, D. B., Casey, C. M., et al. 2015, ApJ, 801, 80
Le Floc'h, E., Aussel, H., Ilbert, O., et al. 2009, ApJ, 703, 222
Leroy, A. K., Bolatto, A., Gordon, K., et al. 2011, ApJ, 737, 12
Lutz, D., Poglitsch, A., Altieri, B., et al. 2011, A&A, 532, A90
Madau, P., & Dickinson, M. 2014, ARA&A, 52, 415
Magdis, G. E., Daddi, E., Béthermin, M., et al. 2012, ApJ, 760, 6
Magnelli, B., Lutz, D., Saintonge, A., et al. 2014, A&A, 561, A86
Maller, A. H., Berlind, A. A., Blanton, M. R., & Hogg, D. W. 2009, ApJ, 691,
    394
Masters, K. L., Nichol, R., Bamford, S., et al. 2010, MNRAS, 404, 792
Mateos, S., Alonso-Herrero, A., Carrera, F. J., et al. 2012, MNRAS, 426, 3271
Mathis, J. S. 1990, ARA&A, 28, 37
McLure, R. J., Dunlop, J. S., Cullen, F., et al. 2018, MNRAS, 476, 3991
Misiriotis, A., Popescu, C. C., Tuffs, R., & Kylafis, N. 2001, A&A, 372, 775
Möllenhoff, C., Popescu, C. C., & Tuffs, R. J. 2006, A&A, 456, 941
Molnar, D. C., Sargent, M. T., Delhaize, J., et al. 2018, MNRAS, 475, 827
Moriondo, G., Giovanelli, R., & Haynes, M. P. 1998, A&A, 338, 795
Morselli, L., Renzini, A., Popesso, P., & Erfanianfar, G. 2016, MNRAS, 462,
    2355
Moshir, M., Kopan, G., Conrow, T., et al. 1990, Bull. Am. Astron. Soc., 22, 1325
Moustakas, J., & Kennicutt, Jr. R. C. 2006, ApJS, 164, 81
Muñoz-Mateos, J. C., Gil de Paz, A., Boissier, S., et al. 2009, ApJ, 701, 1965
Murphy, E. J., Condon, J. J., Schinnerer, E., et al. 2011, ApJ, 737, 67
Nelson, D., Pillepich, A., Springel, V., et al. 2018, MNRAS, 475, 624
Noeske, K. G., Weiner, B. J., Faber, S. M., et al. 2007, ApJ, 660, L43
Padmanabhan, N., Schlegel, D. J., Finkbeiner, D. P., et al. 2008, ApJ, 674, 1217
Pannella, M., Carilli, C. L., Daddi, E., et al. 2009, ApJ, 698, L116
Pannella, M., Elbaz, D., Daddi, E., et al. 2015, ApJ, 807, 141

Patel, S. G., Holden, B. P., Kelson, D. D., et al. 2012, ApJ, 748, L27
Peek, J. E. G., & Schiminovich, D. 2013, ApJ, 771, 68
Peletier, R. F., & Willner, S. P. 1992, AJ, 103, 1761
Pérez-González, P. G., Kennicutt, Jr. R. C., Gordon, K. D., et al. 2006, ApJ, 648,
    987
Poglitsch, A., Waelkens, C., Geis, N., et al. 2010, A&A, 518, L2
Popescu, C. C., & Tuffs, R. J. 2008, AIP Conf. Ser., eds. V. Mioc, C. Dumitrche,
    & N. A. Popescu, 1043, 380
Popescu, C. C., Misiriotis, A., Kylafis, N. D., Tuffs, R. J., & Fischera, J. 2000,
    A&A, 362, 138
Popescu, C. C., Tuffs, R. J., Madore, B. F., et al. 2005, ApJ, 619, L75
Popescu, C. C., Tuffs, R. J., Dopita, M. A., et al. 2011, A&A, 527, A109
Popping, G., Somerville, R. S., & Galametz, M. 2017, MNRAS, 471, 3152
Reddy, N. A., Erb, D. K., Pettini, M., Steidel, C. C., & Shapley, A. E. 2010, ApJ,
    712, 1070
Reddy, N., Dickinson, M., Elbaz, D., et al. 2012, ApJ, 744, 154
Rémy-Ruyer, A., Madden, S. C., Galliano, F., et al. 2014, A&A, 563, A31
Rowlands, K., Dunne, L., Dye, S., et al. 2014, MNRAS, 441, 1017
Salim, S., Lee, J. C., Janowiecki, S., et al. 2016, ApJS, 227, 2
Salmi, F., Daddi, E., Elbaz, D., et al. 2012, ApJ, 754, L14
Sanders, D. B., Salvato, M., Aussel, H., et al. 2007, ApJS, 172, 86
Sandstrom, K. M., Leroy, A. K., Walter, F., et al. 2013, ApJ, 777, 5
Santini, P., Maiolino, R., Magnelli, B., et al. 2014, A&A, 562, A30
Sargent, M. T., Carollo, C. M., Lilly, S. J., et al. 2007, ApJS, 172, 434
Sargent, M. T., Carollo, C. M., Kampczyk, P., et al. 2010, ApJ, 714, L113
Sargent, M. T., Béthermin, M., Daddi, E., & Elbaz, D. 2012, ApJ, 747, L31
Sargent, M. T., Daddi, E., Béthermin, M., et al. 2014, ApJ, 793, 19
Scarlata, C., Carollo, C. M., Lilly, S., et al. 2007, ApJS, 172, 406
Schlegel, D. J., Finkbeiner, D. P., & Davis, M. 1998, ApJ, 500, 525
Schreiber, C., Pannella, M., Elbaz, D., et al. 2015, A&A, 575, A74
Scoville, N., Arnouts, S., Aussel, H., et al. 2013, ApJS, 206, 3
Shao, Z., Xiao, Q., Shen, S., et al. 2007, ApJ, 659, 1159
Simard, L., Willmer, C. N. A., Vogt, N. P., et al. 2002, ApJS, 142, 1
Simard, L., Mendel, J. T., Patton, D. R., Ellison, S. L., & McConnachie, A. W.
    2011, ApJS, 196, 11
Smith, D. J. B., Dunne, L., da Cunha, E., et al. 2012, MNRAS, 427, 703
Smith, M. W. L., Eales, S. A., De Looze, I., et al. 2016, MNRAS, 462, 331
Smolčić, V., Delvecchio, I., Zamorani, G., et al. 2017a, A&A, 602, A2
Smolčić, V., Novak, M., Bondi, M., et al. 2017b, A&A, 602, A1
Speagle, J. S., Steinhardt, C. L., Capak, P. L., & Silverman, J. D. 2014, ApJS,
    214, 15
Tacchella, S., Carollo, C. M., Forster Schreiber, N. M., et al. 2018, ApJ, 859,
    56
Tacconi, L. J., Neri, R., Genzel, R., et al. 2013, ApJ, 768, 74
Tacconi, L. J., Genzel, R., Saintonge, A., et al. 2018, ApJ, 853, 179
Tasca, L. A. M., Le Fèvre, O., Hathi, N. P., et al. 2015, A&A, 581, A54
Taylor, E. N., Hopkins, A. M., Baldry, I. K., et al. 2011, MNRAS, 418, 1587
Taylor, M.-B. 2005, Astronomical Data Analysis Software and Systems XIV,
    347, 29
Travis, E. O. 2006, A guide to NumPy (USA: Trelgol Publishing)
Trayford, J. W., Camps, P., Theuns, T., et al. 2017, MNRAS, 470, 771
Tuffs, R. J., Popescu, C. C., Völk, H. J., Kylafis, N. D., & Dopita, M. A. 2004,
    A&A, 419, 821
Tully, R. B., Pierce, M. J., Huang, J.-S., et al. 1998, AJ, 115, 2264
Valentijn, E. A. 1990, Nature, 346, 153
Wang, L., Norberg, P., Gunawardhana, M. L. P., et al. 2016, MNRAS, 461, 1898
Wang, W., Faber, S. M., Liu, F. S., et al. 2017, MNRAS, 469, 4063
Whitaker, K. E., Franx, M., Leja, J., et al. 2014, ApJ, 795, 104
Whitaker, K. E., Franx, M., Bezanson, R., et al. 2015, ApJ, 811, L12
Whitaker, K. E., Pope, A., Cybulski, R., et al. 2017, ApJ, 850, 208
White, III, R. E., Keel, W. C., & Conselice, C. J. 2000, ApJ, 542, 761
Williams, R. J., Quadri, R. F., Franx, M., van Dokkum, P., & Labbé, I. 2009,
    ApJ, 691, 1879
Williams, R. J., Quadri, R. F., Franx, M., et al. 2010, ApJ, 713, 738
Wisnioski, E., Förster Schreiber, N. M., Wuyts, S., et al. 2015, ApJ, 799, 209
Wright, E. L., Eisenhardt, P. R. M., Mainzer, A. K., et al. 2010, AJ, 140, 1868
Wuyts, S., Labbé, I., Förster Schreiber, N. M., et al. 2008, ApJ, 682, 985
Wuyts, S., Förster Schreiber, N. M., Lutz, D., et al. 2011a, ApJ, 738, 106
Wuyts, S., Förster Schreiber, N. M., van der Wel, A., et al. 2011b, ApJ, 742,
    96
Xilouris, E. M., Byun, Y. I., Kylafis, N. D., Paleologou, E. V., & Papamastorakis,
    J. 1999, A&A, 344, 868
Yip, C.-W., Szalay, A. S., Wyse, R. F. G., et al. 2010, ApJ, 709, 780
Yuan, Q.-r., & Zhu, C.-x. 2004, Chinese Astron. Astrophys., 28, 127
Zahid, H. J., Dima, G. I., Kewley, L. J., Erb, D. K., & Davé, R. 2012, ApJ, 757,
    54
Zahid, H. J., Dima, G. I., Kudritzki, R.-P., et al. 2014, ApJ, 791, 130
Zamojski, M. A., Schiminovich, D., Rich, R. M., et al. 2007, ApJS, 172, 468

Appendix A: Choice of normalisation

Systematic uncertainties in our analysis arise from the normalisation factor adopted to represent the expected "true" SFR of our galaxies. Here we discuss how our results change as a result of different choices for normalisation; we do not account for all possible differences, but rather focus on a few cases.

A.1. Choice of main sequence

Many different MS relations exist in the literature. Different methods for selecting "star-forming" galaxies tend to produce different results (Karim et al. 2011; Speagle et al. 2014). Other differences such as assumed IMF, SFR calibration, and different SED inputs such as star formation histories also make comparisons between studies challenging. Studies such as Schreiber et al. (2015), Lee et al. (2015) and Whitaker et al. (2014), report a turnover or flattening in the galaxy main sequence at high-stellar mass ($\log(M_*/M_\odot) > 10.3$). The origin of the turnover could be due to samples that include more bulge-dominated galaxies, which lie below the main sequence that is defined for pure disk-dominated galaxies (e.g. Salmi et al. 2012; Lang et al. 2014; Whitaker et al. 2015). Figure A.1 is a visualisation of different MS relations from the literature, including the relations used in this work, at $z \sim 0$ (the relations with lower SFRs) and at $z \sim 0.7$ (higher SFRs). We investigate how our results change when using different main-sequence relations.

Speagle et al. (2014) compiled 25 studies from the literature and found a consensus MS relation after converting all observations to a common set of calibrations. We use the best fit

$$\log(\text{SFR}_{\text{MS}}) = (0.84 - 0.026t)\log(M_*) - (6.51 - 0.11t), \quad \text{(A.1)}$$

where t is the age of the universe in Gyr. Speagle et al. (2014) removed data with $t < 2.5$ Gyr (and $t > 11.5$ Gyr) from their analysis. Their reasons for removing the low-redshift data is because most local studies have been based on the SDSS and most measurements require some aperture corrections. In Fig. A.1, we show Eq. (A.1) extrapolated to the redshift of our local sample, $0.04 < z < 0.1$ is shown in shaded green.

Schreiber et al. (2015) use a method called "scatter stacking" and combine direct UV and FIR light for a mass-complete sample of star-forming galaxies and find a close-to-linear slope of the relation but allow for an observed flattening of the MS that takes places at masses $\log(M_*/M_\odot) > 10.5$ at low redshift. Schreiber et al. (2015) found the following equation to represent the locus of the MS:

$$\log(\text{SFR}_{\text{MS}}) = m - 0.5 + 1.5\log(1 + z)$$
$$- 0.3\left[\max(0, m - 0.36 - 2.5\log(1 + z))\right]^2, \quad \text{(A.2)}$$

where $m = \log(M_*/10^9 M_\odot)$. The error bars in Eqs. (A.1) and (A.2) were omitted because we did not incorporate them in our SFR-inclination analysis. Figure A.1 shows the Schreiber et al. (2015) MS relation at the redshifts considered for this analysis. The lowest redshift considered in the Schreiber et al. (2015) analysis was $z = 0.3$, therefore the low-redshift relation is also an extrapolation of the data.

For our main analysis, we adopted an updated MS relationship based off an inter-sample "concordance" analysis by Sargent et al. (2014), which unlike the compiled relation by Speagle et al.
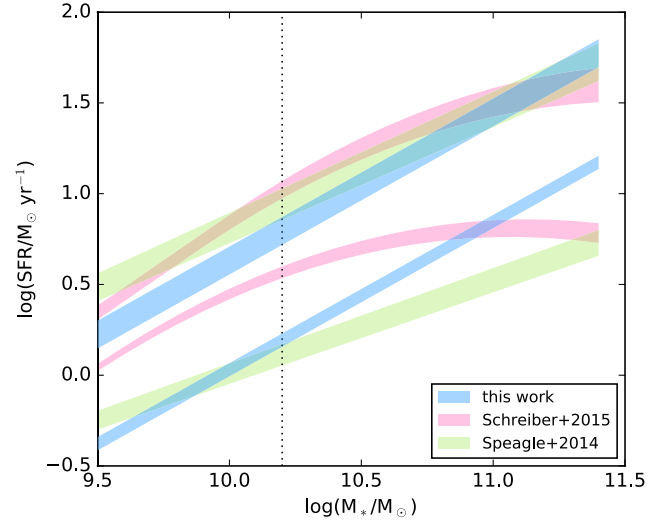

Fig. A.1. Main sequence relations at our two redshift slices. For our analysis we adopt the MS given by Eq. (9) (blue), but we also compare to MS relations with a shallower slope, (Speagle et al. 2014; green) and a MS relation with a turn-over at low redshifts and high stellar masses, Schreiber et al. (2015). The vertical dotted line at $\log(M_*/M_\odot) = 10.2$ shows the mass cut used in this work. We note that the Speagle et al. (2014) and Schreiber et al. (2015) relations shown for comparison were not calibrated at $z = 0$.

(2014), includes local studies such as Chang et al. (2015) for constraining the MS evolution.

Table A.1 gives the alternative results for our analysis in Sect. 3 normalising to these alternative MS equations. The fitted slope of the $\text{SFR}_{\text{UV}}/\text{SFR}_{\text{MS}}$ versus inclination of our local or $z \sim 0.7$ samples relation does depend significantly on the MS normalisation selected. On the other hand, the intercept values are different. For the $z \sim 0.7$ sample, the intercepts are lower than our adopted MS result for the Speagle and lowest for the Schreiber normalisation. For our $z \sim 0$ sample, the intercept is lowest for the Schreiber MS, and highest for the Speagle MS. These results are not surprising considering the normalisation differences seen the MS relations in Fig. A.1.

Using the Speagle et al. (2014) MS for normalisation of the SFR_{UV} gives best fitting parameters for the Tuffs et al. (2004) models $\tau_{B,z=0}^f = 3.19_{-0.08}^{+0.1}$, $F_{z=0} = 0.02_{-0.01}^{+0.01}$ for the local galaxy sample, and $\tau_{B,z=0.7}^f = 4.6_{-1.5}^{+1.3}$, $F_{z=0.7} = 0.57_{-0.03}^{+0.04}$ for our COSMOS sample.

On the other hand, using the Schreiber et al. (2015) MS results in $\tau_{B,z=0}^f = 2.89_{-0.1}^{+0.1}$, $F_{z=0} = 0.48_{-0.006}^{+0.005}$ and $\tau_{B,z=0.7}^f = 5.4_{-1.2}^{+0.8}$, $F_{z=0.7} = 0.58_{-0.03}^{+0.02}$.

In these cases, the face-on B-band optical depth increases from $z \sim 0$ to $z \sim 0.7$ as well as the clumpiness factor (which increases by a factor of ~28 for the Speagle et al. 2014 MS, and by a factor 1.2 for the Schreiber et al. 2015 MS).

A.2. Attenuation–inclination relations normalised by galaxy SFR_{MIR}

We investigate the effects that normalising the UV, radio and FIR SFRs by the MIR SFR (12 μm at $z \sim 0$ and 24 μm at $z \sim 0.7$), rather than the MS SFR, has on our analysis. By using $\text{SFR}_\lambda/\text{SFR}_{\text{MIR}}$ for our inclination analysis, we remove potential systematic effects related to the M_* dependence of the star-forming MS (as discussed above). SFR_{MIR} has the practical advantage as the normalising factor (over e.g. SFR_{FIR}) in that

Table A.1. Best fit parameters of the SFR vs. inclination relation under different SFR normalisations.

λ	This MS		Speagle MS		Schreiber MS		MIR	
	Slope	Intercept	Slope	Intercept	Slope	Intercept	Slope	Intercept
$\mathrm{SFR}_{UV}\ z \sim 0$	$-0.78\,^{+0.08}_{-0.09}$	$-0.20\,^{+0.04}_{-0.03}$	$-0.76\,^{+0.07}_{-0.08}$	$-0.11\,^{+0.03}_{-0.03}$	$-0.75\,^{+0.08}_{-0.08}$	$-0.54\,^{+0.03}_{-0.03}$	$-0.59^{+0.10}_{-0.09}$	$-0.27^{+0.03}_{-0.03}$
$\mathrm{SFR}_{MIR}\ z \sim 0$	$-0.12\,^{+0.03}_{-0.02}$	$0.05\,^{+0.01}_{-0.01}$	$-0.10\,^{+0.02}_{-0.02}$	$0.14\,^{+0.01}_{-0.01}$	$-0.08\,^{+0.02}_{-0.03}$	$-0.29\,^{+0.01}_{-0.01}$	$-$	$-$
$\mathrm{SFR}_{FIR}\ z \sim 0$	$-0.06\,^{+0.22}_{-0.20}$	$0.68\,^{+0.09}_{-0.09}$	$-0.02\,^{+0.19}_{-0.18}$	$0.81\,^{+0.08}_{-0.08}$	$0.04\,^{+0.19}_{-0.17}$	$0.40\,^{+0.08}_{-0.08}$	$0.05^{+0.16}_{-0.16}$	$0.26\,^{+0.08}_{-0.08}$
$\mathrm{SFR}_{radio}\ z \sim 0$	$-0.10\,^{+0.20}_{-0.22}$	$0.52\,^{+0.11}_{-0.09}$	$-0.09\,^{+0.20}_{-0.17}$	$0.69\,^{+0.09}_{-0.09}$	$-0.07\,^{+0.16}_{-0.19}$	$0.31\,^{+0.10}_{-0.09}$	$0.23^{+0.21}_{-0.21}$	$-0.07^{+0.12}_{-0.24}$
$\mathrm{SFR}_{UV}\ z \sim 0.7$	$-0.54\,^{+0.18}_{-0.17}$	$-0.74\,^{+0.08}_{-0.08}$	$-0.59\,^{+0.17}_{-0.18}$	$-0.85\,^{+0.09}_{-0.07}$	$-0.59\,^{+0.17}_{-0.17}$	$-0.94\,^{+0.08}_{-0.08}$	$-0.60^{+0.23}_{-0.21}$	$-1.00^{+0.09}_{-0.1}$
$\mathrm{SFR}_{MIR}\ z \sim 0.7$	$-0.03\,^{+0.10}_{-0.09}$	$0.28\,^{+0.05}_{-0.05}$	$-0.05\,^{+0.10}_{-0.10}$	$0.16\,^{+0.06}_{-0.05}$	$-0.04\,^{+0.09}_{-0.10}$	$0.06\,^{+0.05}_{-0.05}$	$-$	$-$
$\mathrm{SFR}_{FIR}\ z \sim 0.7$	$-0.02\,^{+0.23}_{-0.25}$	$0.54\,^{+0.15}_{-0.13}$	$-0.03\,^{+0.23}_{-0.21}$	$0.43\,^{+0.12}_{-0.13}$	$-0.03\,^{+0.22}_{-0.23}$	$0.33\,^{+0.13}_{-0.12}$	$0.16\,^{+0.1}_{-0.14}$	$-0.02^{+0.08}_{-0.11}$
$\mathrm{SFR}_{radio}\ z \sim 0.7$	$-0.17\,^{+0.31}_{-0.33}$	$0.68\,^{+0.19}_{-0.18}$	$-0.14\,^{+0.27}_{-0.32}$	$0.55\,^{+0.18}_{-0.15}$	$-0.13\,^{+0.30}_{-0.30}$	$0.45\,^{+0.18}_{-0.15}$	$0.29\,^{+0.18}_{-0.20}$	$-0.05^{+0.11}_{-0.10}$

Notes. Column 1 is a repeat of Table 3 (to facilitate comparison), Cols. 2 and 3 show the best fitting parameters obtained when using the Speagle et al. (2014) and Schreiber et al. (2015) MS relations to normalise the SFR. Column 4 shows the best-fit parameters when the SFR of each galaxy is normalised by its MIR SFR.

most of our SDSS and COSMOS galaxies are detected in the WISE and MIPS data-sets, respectively.

Attenuation–inclination relations derived using this alternative normalisation are consistent with our results obtained using the MS normalisation, with the exception of a few cases which we will now discuss.

The slightly positive slope (0.23 ± 0.21) of the SDSS radio sample is partially due to the fact that the local $\mathrm{SFR}_{12\mu m}$ has a slight negative trend with inclination (-0.12 ± 0.02), and so normalising by the 12 μm SFR will induce a slight positive slope. The distributions of the FUV slopes now have consistent medians. This could also be in part because the local MIR slope is slightly negative so normalising by the 12 μm SFR will shift the local UV slope. However, this shift of ~ 0.12 would not be enough to fully explain the change in local UV slopes (from -0.78 ± 0.08 to -0.59 ± 0.1) when using a MS or $\mathrm{SFR}_{12\mu m}$ normalisation. Additionally, the COSMOS SFR_{UV} slope changes from -0.53 ± 0.17 to -0.6 ± 0.23. The local 60 μm intercept is greater than zero. This corresponds to a difference between the 60 μm and 12 μm SFR calibrations that we discuss in Appendix B.

$\mathrm{SFR}/\mathrm{SFR}_{MS}$ will vary from galaxy to galaxy as there is an intrinsic scatter to the MS (Speagle et al. 2014; Schreiber et al. 2015). We find that the scatter of the $\mathrm{SFR}_{UV}/\mathrm{SFR}_{MS}$-inclination relation is similar to the scatter of the $\mathrm{SFR}_{UV}/\mathrm{SFR}_{12\mu m}$ relation (in fact the $\mathrm{SFR}_{UV}/\mathrm{SFR}_{12\mu m}$ ratio shows larger scatter). This is not surprising because the amount of UV emission that escapes will depend, amongst other things, on the star-dust geometry, inclination angle, and the dust mass as well as the SFR. Therefore the $\mathrm{SFR}_{12\mu m}$ is not readily correlated to the SFR_{UV}, even for our sample that has been selected to have similar M_*, n, and $r_{1/2}$.

Appendix B: Comparison of SFR tracers

Figure B.1 shows how the multiwavelength SFRs of galaxies used for our analysis compare in the cases where galaxies are detected in the relevant bands. It is important to recognise that these different SFR tracers come from emission produced in different regions (from the HII regions, dust, supernovae remnants) and trace processes on different timescales. FUV, TIR, 24 μm and 1.4 GHz emission come from stellar populations 0–100 Myr

old (Kennicutt & Evans 2012), but the values are sensitive to the star formation history.

We fit a linear function to relate the logarithmic SFRs using the same fitting and resampling techniques used in Sect. 3. However, in this case, we re-sample the data N times, where N is the number of galaxies in our sample detected at both wavelengths. The best fit lines from each re-sampled data-set are shown as magenta lines in Fig. B.1. We report the median and error bars (given by the 5th and 95th percentile) in the equations below. The numbers in the brackets show the number of galaxies available for the fit.

$$\log(\mathrm{SFR}_{UV}) = 0.31^{+0.04}_{-0.06} \log(\mathrm{SFR}_{MIR}) + 0.44^{+0.01}_{-0.01} \quad (1019)$$

$$\log(\mathrm{SFR}_{UV}) = 0.1^{+0.1}_{-0.5} \log(\mathrm{SFR}_{FIR}) + 1.0^{+0.1}_{-0.2} \quad (20)$$

$$\log(\mathrm{SFR}_{UV}) = 0.2^{+0.4}_{-0.1} \log(\mathrm{SFR}_{1.4GHz}) + 1.09^{+0.05}_{-0.07} \quad (14)$$

$$\log(\mathrm{SFR}_{MIR}) = 0.79^{+0.08}_{-0.08} \log(\mathrm{SFR}_{FIR}) + 0.38^{+0.07}_{-0.07} \quad (290)$$

$$\log(\mathrm{SFR}_{MIR}) = 0.56^{+0.15}_{-0.07} \log(\mathrm{SFR}_{1.4GHz}) + 0.4^{+0.1}_{-0.1} \quad (83)$$

$$\log(\mathrm{SFR}_{FIR}) = 0.53^{+0.07}_{-0.10} \log(\mathrm{SFR}_{1.4GHz}) + 0.3^{+0.1}_{-0.1} \quad (83)$$

COSMOS $z \sim 0.7$ results:

$$\log(\mathrm{SFR}_{UV}) = 0.15^{+0.09}_{-0.08} \log(\mathrm{SFR}_{MIR}) + 1.30^{+0.03}_{-0.03} \quad (277)$$

$$\log(\mathrm{SFR}_{UV}) = 0.04^{+0.1}_{-0.1} \log(\mathrm{SFR}_{FIR}) + 1.62^{+0.05}_{-0.05} \quad (65)$$

$$\log(\mathrm{SFR}_{UV}) = 0.2^{+0.1}_{-0.2} \log(\mathrm{SFR}_{3GHz}) + 1.74^{+0.04}_{-0.05} \quad (35)$$

$$\log(\mathrm{SFR}_{MIR}) = 0.7^{+0.2}_{-0.2} \log(\mathrm{SFR}_{FIR}) + 0.5^{+0.4}_{-0.4} \quad (85)$$

$$\log(\mathrm{SFR}_{MIR}) = 0.8^{+0.2}_{-0.1} \log(\mathrm{SFR}_{3GHz}) + 0.5^{-0.4}_{+0.3} \quad (41)$$

$$\log(\mathrm{SFR}_{FIR}) = 0.6^{+0.2}_{-0.2} \log(\mathrm{SFR}_{3GHz}) + 0.7^{+0.3}_{-0.3} \quad (41)$$

A large scatter exists between the SFR_{UV} and longer wavelength SFR tracers. The UV suffers from dust attenuation that is dependent on viewing angle amongst other factors. The data in Fig. B.1 are coloured by their inclination angle, and it is clear that the SFR_{UV} strongly depends on inclination. Face-on galaxies ($1 - \cos(i) = 0$) having SFR_{UV} that lie closer to $\mathrm{SFR}_{12\mu m}$ values in the local sample. However, in almost all galaxies, in both the local and COSMOS samples, $\mathrm{SFR}_{UV} < \mathrm{SFR}_{MIR}$ as there will
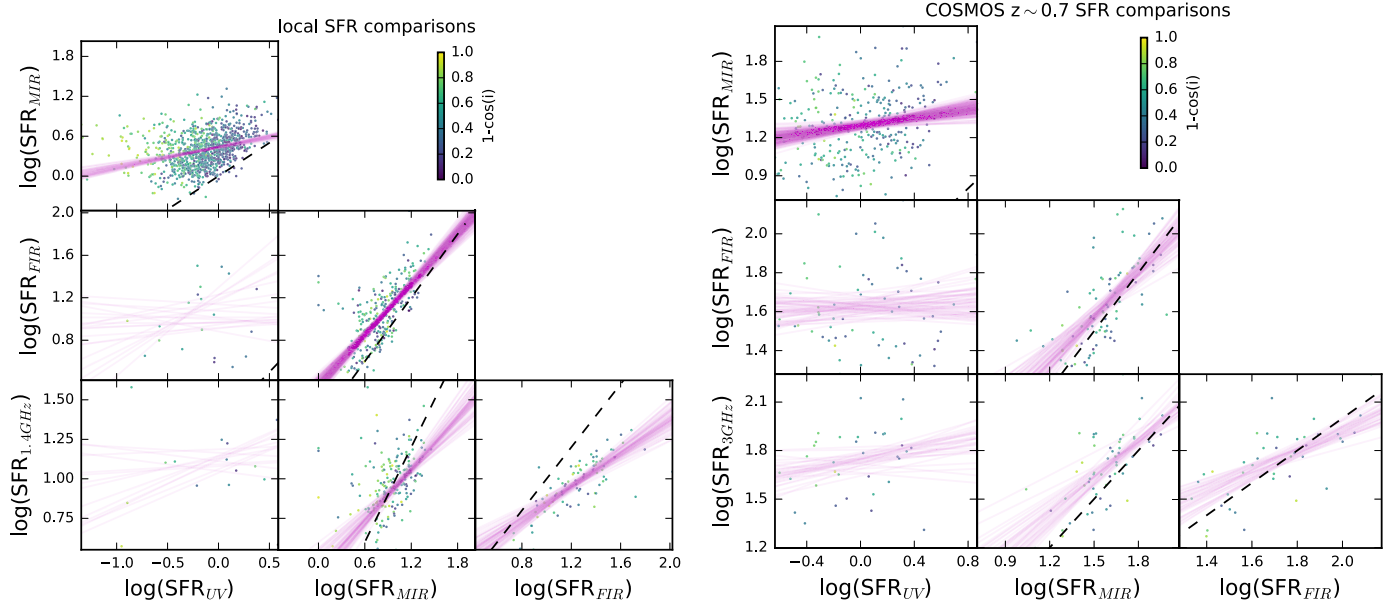
Fig. B.1. Comparison of the SFRs derived using the different monochromatic calibrations used in this paper and described in Sect. 2.5. The dashed line represents the one-to-one line. Magenta lines show best fit linear relations to resampled data, with the number of fits shown equal to the number of galaxies in each panel. The SFR_{UV} is not corrected for dust attenuation and so is expected to be smaller than the other indicators. Data are colour-coded by galaxy inclination angle.

be some level of FUV attenuation even for face-on galaxies (as discussed in Sects. 3.2 and 4).

In the COSMOS sample at $z \sim 0.7$, we find a good agreement between the 24 μm, 100 μm, and 3 GHz SFRs. This is encouraging as all three are tied to TIR calibration (through SED fitting or via the IR-radio correlation). Locally the SFR_{FIR} is greater than the SFRs derived from 12 μm and 1.4 GHz. The 1.4 GHz SFR calibration of Davies et al. (2017) used for the local sample depends sub-linearly on SFR. Therefore it follows that 60 μm SFR is higher than the 1.4 GHz SFR because there is a linear relation between 1.4 GHz and FIR (FIRRC). However, this would imply that the FIR emission traced by 60 μm does not correlate linearly with SFR. On the other hand, our best fits show that $SFR_{12\mu m}$ is also larger than $SFR_{1.4GHz}$ at high SFRs. This could imply that the $SFR_{1.4GHz}$ relation used by Davies et al. (2017) underestimates the SFR.

Appendix C: Evolution of UV attenuation with redshift: studies included in Fig. 7

Bouwens et al. (2016) give a "consensus relationship" for IRX-M_* between $2 < z < 3$ by combining the results of Whitaker et al. (2014), Reddy et al. (2010), and Álvarez-Márquez et al. (2016). In Fig. 7, we show the resulting FUV attenuation obtained by evaluating the "consensus" equation at $\log(M_*/M_\odot) = 10.2$–10.6. McLure et al. (2018) fit of the $A_{1600} - M_*$ relation found and IRX-M_* relation for star-forming galaxies in the *Hubble* Ultra Deep field is well described by a Calzetti et al. (2000) attenuation law. As done for Bouwens et al. (2016), we show the expected SFR_{UV}/SFR_{tot} for galaxies with M_* ranging from $10^{10.2}$ to $10^{11.4} M_\odot$ according to the IRX-M_* fit of McLure et al. (2018) as a shaded region.

Whitaker et al. (2014) report the average L_{IR}, L_{UV} and SFRs for SF galaxies selected via colour–colour criteria in the CANDELs fields in bins of stellar mass and redshift. From these values we calculate SFR_{UV}/SFR_{tot} and in Fig. 7 we

show the minimum and maximum values found for galaxies with $10.2 < \log(M_*/M_\odot) < 11.4$ (to match this work). For Wuyts et al. (2011b) we read off the SFR_{UV}/SFR_{IR} fraction at the position of the MS at $\log(M_*/M_\odot) = 10.2$, 10.8, and 11.4 from their Fig. 6. Their MS was approximated with a constant slope of 1. We consider the total SFR to be $SFR_{UV} + SFR_{IR}$ and then solve for SFR_{UV}/SFR_{tot}. The error bars show the range corresponding to the Wuyts et al. (2011b) results at the different stellar masses spanned by this work.

Wang et al. (2016) give the observed uncorrected FUV luminosity and corrected luminosities for galaxies in their Fig. 9 for a sample of galaxies in GAMA/H-ATLAS with slightly lower masses than our sample, median $\log(M_*/M_\odot) = 10.13$, and a median redshift $z = 0.077$.

Pannella et al. (2009) use BzK selection to perform a stacking analysis on 1.4 GHz data to infer the total SFR at $z \sim 2$. Panella report the attenuation at 1500 Å, derived from the stacked $SFR_{FUV}/SFR_{1.4GHz}$, as a function of stellar mass. In Fig. 7, we include the results from 10.2 to 11.4 as indicated by the error-bars. Pannella et al. (2015) take a mass-complete sample of galaxies in GOODS-N classified as star forming by a UVJ colour–colour selection. We take measurements of A_{FUV} at $10.2 < \log(M_*/M_\odot) < 11.4$ from Fig. 7 in Pannella et al. (2015). They find that A_{FUV} increases by 0.3 dex from $z \sim 0.7$ to $z \sim 1$ and then stays constant out to $z \sim 3.3$.

Burgarella et al. (2013) and Cucciati et al. (2012) use a ratio of UV and FIR luminosity functions in the VIMOS-VLT Deep Survey to calculate A_{FUV}. This considers galaxies of all stellar masses. The difference between these studies is that Burgarella et al. (2013) uses a PACS-selected sample and Cucciati et al. (2012) use an I-band selected catalogue.

Reddy et al. (2012) use *Herschel* measurements of UV-selected star-forming $1.6 < z < 2.6$ galaxies in GOODS-North. In Fig. 7, we show the SFR_{UV}/SFR_{tot} for their samples A (All UV-selected galaxies) and E (Ultra-Luminous Infrared Galaxies; ULIRGs), where the ULIRG sample has SFR_{UV}/SFR_{tot} ratios

consistent with massive galaxies. Heinis et al. (2013) calculated $A_{\rm FUV}$ for a UV-selected sample of galaxies $1.2 < z < 1.7$ from IR and UV data. Dahlen et al. (2007) draw on GOODS-South photometry to measure the rest-frame 1500 and 2800 Å luminosity functions. The UV slope is used, assuming the Calzetti attenuation law to calculate the FUV attenuation correction factor required.

Hao et al. (2011) use a number of normal star-forming nearby galaxies from Kennicutt et al. (2003) and Moustakas & Kennicutt (2006). The sample has $\log({\rm SFR}/M_{\odot}{\rm yr}^{-1})$ values from -3 to 1. Calzetti et al. (2000) combined IR and UV data for a sample of eight nearby galaxies with $\log({\rm SFR}/M_{\odot}{\rm yr}^{-1})$ ranging from -1 to 1.7.

Buat et al. (2015) calculate the FUV attenuation of IR-selected galaxies from $z \sim 0.2$ to $z \sim 2$ by fitting galaxy SEDs from UV to IR wavelengths. They conclude that galaxies selected in the IR show larger attenuation than galaxies selected in the UV or optical as they are the more massive galaxies (average $M_* > 10^{10.4} M_{\odot}$). In Fig. 7, we show the average $A_{\rm FUV}$ for each redshift bin quoted in Table 3 of Buat et al. (2015). The error bars show the sample dispersion of 1.3 mags.